

RAMSES: German Meteorological Service autonomous Raman lidar for water vapor, temperature, aerosol, and cloud measurements

Jens Reichardt,^{1,*} Ulla Wandinger,² Volker Klein,³ Ina Mattis,^{2,4}
Bernhard Hilber,⁵ and Robert Begbie¹

¹Richard-Aßmann-Observatorium, Deutscher Wetterdienst, Am Observatorium 12, Lindenberg 15848, Germany

²Leibniz Institute for Tropospheric Research, Permoserstr. 15, Leipzig 04318, Germany

³Kayser-Threde GmbH, Wolfratshauser Str. 48, München 81379, Germany

⁴Meteorologisches Observatorium Hohenpeißenberg, Deutscher Wetterdienst,
Albin-Schwaiger-Weg 10, Hohenpeißenberg 82383, Germany

⁵Loritus GmbH, Bruderstr. 3, München 80538, Germany

*Corresponding author: jens.reichardt@dwd.de

Received 30 March 2012; revised 13 July 2012; accepted 21 August 2012;
posted 5 October 2012 (Doc. ID 165833); published 28 November 2012

The Raman lidar for atmospheric moisture sensing (RAMSES) for unattended, continuous multiparameter atmospheric profiling is presented. A seeded frequency-tripled Nd:YAG laser serves as the light source. A nine-channel polychromator, nonfiber coupled to the main telescope (790 mm diameter), is used for far-range measurements. Near-range observations are performed with a three-channel polychromator, fiber coupled to a secondary telescope (200 mm diameter). Measurement parameters are water-vapor mixing ratio (MR), temperature, and the optical particle parameters, which are extinction coefficient, backscatter coefficient, lidar ratio, and depolarization ratio at 355 nm. Profiles of water-vapor MR are measured from close to the surface up to 14 km at night and 5 km during the day under favorable atmospheric conditions in 20 min. Temperature profiles of the troposphere and lower stratosphere are determined with the rotational-Raman technique. For the detection of the rotational Raman signals, a new beamsplitter/interference-filter experimental setup is implemented that is compact, robust, and easy to align. Furthermore, the polychromator design allows two independent methods for calibrating measurements of depolarization ratio. RAMSES optical design concept and experimental setup are detailed, and a description of the operational near-real-time data evaluation software is given. A multiday observation is discussed to illustrate the measurement capabilities of RAMSES. © 2012 Optical Society of America

OCIS codes: 280.0280, 280.3640, 010.1280, 280.6780, 290.1090, 010.3920.

1. Introduction

Since the 1990s, Raman lidars have evolved into powerful instruments for atmospheric research. Next to their relatively modest experimental complexity and multiparameter capability, one advantage

that makes Raman lidars particularly conducive for meteorological and climatological studies is that they allow humidity measurements from the ground to the tropopause and beyond [1]. So unsurprisingly, several high-performance water-vapor Raman lidars have been built over the years, e.g., the instruments described in [2–11] (for a review of preceding pioneering studies see [1,3]). Of the earlier lidars, the Cloud and Radiation Testbed Raman

Lidar CARL [5] at the Atmospheric Radiation Measurement program's Southern Great Plains site in Oklahoma, USA, stood out because it added another layer of complexity, i.e., it was monitoring tropospheric humidity and clouds continuously and autonomously. Its success enticed meteorological services around the world to develop and operate similar instruments, e.g., in Switzerland [12] and Germany.

In 2005, the German Meteorological Service (DWD) complemented the suite of remote-sensing instruments of its Richard Aßmann Observatory at Lindenberg, Brandenburg, with the automated water-vapor Raman lidar system RAMSES (Raman lidar for atmospheric moisture sensing). The early technical design of the lidar [13] allowed high-quality measurements on a routine basis [14], but the range of application was limited because (1) the lidar operated only at night and (2) the set of measured parameters was restricted. In 2009/10 RAMSES was therefore redesigned and expanded to become a powerful day- and night-time multi-parameter Raman lidar for long-term monitoring of the atmosphere. Operational since spring 2010, RAMSES is now routinely measuring the water-vapor profile from close to the surface to the tropopause, tropospheric and stratospheric temperatures, and the full set of optical particle parameters at 355 nm (extinction coefficient, backscatter coefficient, depolarization ratio).

RAMSES engages both in scientific campaigns and long-term investigations. The latter include the validation of numerical weather prediction models and process-oriented studies (which are mainly DWD tasks); the European satellite climatology project [15], for which RAMSES serves as a ground reference site to assist the optimization of retrieval algorithms for spaceborne instruments, as well as to validate the satellite observations in general; and contributions to the activities of the Global Climate Observing System (GCOS) Research Upper Air Network (GRUAN) lead center, which the Richard Aßmann Observatory is since 2007 [16].

In this paper, a comprehensive system description of RAMSES is given. Such an overview seems appropriate at this point, because after years of development and optimization, sketchily documented in [13,17,18], RAMSES has now reached its planned expansion stage. Following the introduction, the technical and optical layout of the instrument is detailed (Section 2). Emphasis is put on the optical system design and on the setup of the RAMSES polychromators, including the implementation of the rotational-Raman temperature method. Other aspects such as systems control and automatization are also discussed. Section 3 describes the operational near-real-time data evaluation software for automated signal processing. A performance evaluation of RAMSES is presented in Section 4. Topics range from signal quality to experience with long-term operation. In Section 5, a multiday observation is discussed to illustrate the measurement capability of

RAMSES in detail. Statistical comparisons between RAMSES and balloon-borne water-vapor instruments are also addressed. The contribution closes with a summary and an outlook.

2. Instrument

A. Instrument Overview

RAMSES is housed in a custom-made thermally insulated 20-foot container. The external chillers and heat exchangers for air conditioning and laser cooling are installed in a shed attached to the container. The roof opening above the telescope is protected with an autonomously operating hatch that, as an additional safety measure independent of the computerized RAMSES system control (see Section 2.C), terminates lidar operation and seals the container in the case of adverse ambient conditions. RAMSES is connected to a standard three-phase/380 V power line (50 Hz). An uninterruptible power supply (UPS) buffers the RAMSES computers during a power failure for about 20 min. After that time, a controlled system shutdown is performed.

The RAMSES optical subsystems are mounted inside a temperature-stabilized (22°C) instrument cabin on a single, solid cross-shaped aluminium construction with its three legs bolted to the 10 mm floor steel plate. The optical bench with the lidar polychromators is placed on the one side of the thermally insulated telescope section, the optical bench with the laser and the transmitter optics on the other side (see Fig. 1). Table 1 summarizes the parameters of the laser transmitter and the receiving telescopes.

RAMSES is equipped with a Continuum Powerlite Precision II 9030 laser system. The frequency-tripled Nd:YAG laser is seeded for wavelength stability

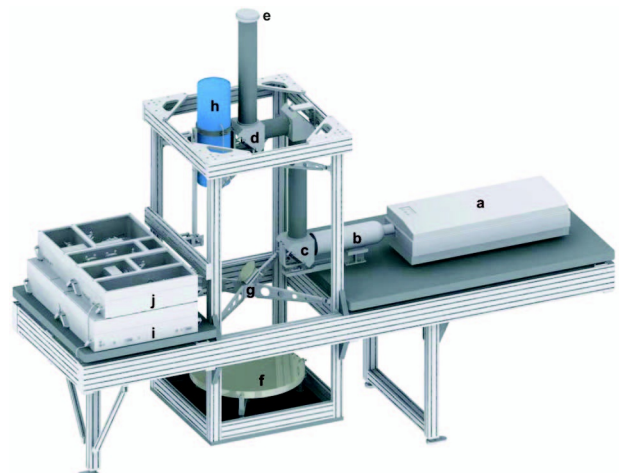


Fig. 1. Overview of the RAMSES lidar setup. a, laser head; b, beam expander; c, motorized beam-steering mirror; d, transmitter mirror mounted on holder of telescope secondary mirror; e, outcoupling window; f, telescope primary mirror; g, deflection mirror; h, near-range telescope; i, far-range polychromator, lower level; j, far-range polychromator, upper level. The fiber-coupled near-range polychromator and the tilted telescope glass shield are not shown.

Table 1. Parameters of the RAMSES Laser Transmitter and Receiving Telescopes

Laser	
Type	Continuum Powerlite Precision II 9030
Seeder system	SI-2000
Pulse energy, 1064 nm	1600 mJ
Pulse energy, 355 nm	450 mJ (operational)
Pulse length, 1064 nm	5–9 ns
Pulse length, 355 nm	3–7 ns
Repetition frequency	30 Hz
Beam divergence	0.5 mrad
Pointing stability	±30 μrad
Transmitted wavelength (in vacuum)	354.825 nm (measured)
Line width	0.003 cm ⁻¹
Beam expander	
Type	Galilean
Beam expansion factor	10
Entrance aperture	12 mm
Exit aperture	120 mm
Beam diameter at entrance	8 mm
Beam diameter at exit	80 mm
Far-range telescope	
Type	Nasmyth-Cassegrain
Primary-mirror diameter	790 mm
Secondary-mirror diameter	203 mm
Effective focal length	6000 mm
Field of view	0.2–1 mrad
Near-range telescope	
Type	Newton with fiber coupling
Mirror diameter	200 mm
Focal length	800 mm
Fiber-coupling lens focal length	75 mm
Distance to primary mirror	760 mm
Effective focal length	522 mm
Fiber diameter	1.7 mm
Distance of optical axis to laser beam	256 mm
Field of view	3.2 mrad

and higher UV performance. Measurements with a WSU/10 laser wavemeter (High Finesse GmbH, Tübingen, Germany) yielded a third-harmonic wavelength of 354.825 nm in vacuum corresponding to 354.71–354.73 nm in air under typical temperature and pressure conditions. Thus an emission wavelength of 354.72 nm was used for the system design. At that wavelength, the laser emits pulses of typically 400–500 mJ with a repetition rate of 30 Hz. The transmitted laser beam is expanded tenfold with a Galilean-type lens telescope (CVI Melles Griot, Albuquerque, New Mexico) in order to limit the beam divergence in the atmosphere to ≤0.1 mrad and to guarantee eye-safety. The first steering mirror after the beam expander is equipped with two microactuators (OWIS GmbH, Staufen, Germany) for active alignment of the laser beam to the optical axis of the far-range receiver (see Section 2.C). The complete transmitter path is encapsulated with aluminium tubes to shield the

receivers from stray light. The laser beam (80 mm diameter) is transmitted vertically (0° zenith angle) through an outcoupling window (fused silica, anti-reflection coated) on the central axis of the far-range receiver telescope.

A Nasmyth-Cassegrain telescope of 790 mm diameter (mirrors provided by Astro-Optik Keller, Neutraubling, Germany) collects the lidar signals for far-range measurements. A folding mirror directs the light toward a nine-channel polychromator unit (channels A–I, see Section 2.B.3) consisting of two levels mounted on each other (Fig. 1). The telescope focus is placed near the entrance of the polychromator unit where a motorized field stop determines the field of view (FOV) of the far-range channels. FOV can be chosen in the range from 0.2 to 1 mrad (field-stop diameters between 1.2 and 6 mm). The exact position of the focal point can be adjusted by slightly varying the distance between the primary and the secondary telescope mirror. Changing the mirror distance by 1 mm moves the focal point by about 9 mm. An adjustment of the field-stop position along the optical axis is also possible. The distance between field stop and telescope focal point is an important parameter for the optimization of the lidar overlap function (see Section 2.B).

A 200 mm Newtonian telescope (Teleskopservice, Putzbrunn, Germany) is used for the near range (heights <3 km). It is mounted within the aperture of the far-range telescope close to the secondary mirror (see Fig. 1). The telescope axis can be tilted against the laser beam. An optical fiber couples the telescope to the near-range polychromator unit with three measurement channels (channels K–M, see Section 2.B.3), which is stacked on top of the far-range polychromator (not shown in Fig. 1). The focal length of the primary mirror of 800 mm is reduced to 560 mm with a fiber-coupling lens of 75 mm focal length in order to realize a FOV of 3.2 mrad and to meet the numerical aperture of the fiber of 0.22.

Both telescopes are shielded from precipitation and, in summer, from insects by a 1 m × 1 m heated glass window (5 mm thick) made of Borofloat 33 (Schott AG, Mainz, Germany) with optical properties similar to optical crown glasses, e.g., BK7. Both the glass window and the inserted laser outcoupling window are tilted by a few degrees to avoid reflections into the laser and the receivers.

The lidar signals are detected with head-on Hamamatsu photomultiplier tubes (PMTs). For the near-range and the far-range channels the R1924P and the R7400U/P-03 tubes were selected, respectively. The latter are housed in PMT modules manufactured by Licel GmbH, Berlin, Germany, of which the two intended for high-altitude measurements are gated to protect the dynode chains from the intense near-range signals. Licel transient recorders are used for data acquisition. All lidar signals are recorded simultaneously in photon-counting mode (250 MHz maximum photon count rate) and analog detection mode (12 bit analog-to-digital converter)

except for the gated signals (photon-counting mode only). The height resolution is 7.5 m, and the height range is 122.88 km.

B. Optical System Design

The entire optical setup of RAMSES was designed and optimized with the commercially available optical ray-tracing software ZEMAX. Major design requirements were

- to optimize the laser-beam receiver-FOV overlap functions for the near-range and far-range receivers in order to cover measurement heights from about 200 m up to 80 km,
- to image the aperture of the far-range primary telescope mirror onto the photocathodes of the far-range receiver channels,
- to optimize transmission properties of all receiver channels under consideration of the polarization state of the backscattered light, and
- to ensure optimum performance of all optical elements by considering polarizing effects of coatings and angular-dependent transmission properties.

1. Overlap Functions and Signal Dynamics

For the ray-tracing calculations, the laser beam was modeled as a function of distance to the receiver telescope. According to the beam diameter and divergence, a circular laser beam cross-section was determined for each calculation distance. Rays from the atmosphere entering the optical receiver started within this area and ended within the receiver entrance aperture. A Monte-Carlo approach with a two-dimensional Gaussian distribution of starting points representing the illumination of the atmospheric disk and an equal distribution of end points was used. From the entrance aperture, the rays were traced through the entire optical setup to the photocathode of the detector.

The receiver optics was modeled as realistic as possible for each receiver channel. The rays were traced through the glass window on the container roof via the telescope mirrors through the field stop and the beam-collimating optics and then further on, depending on the receiver channel, through a number of beamsplitters, polarizing elements, the interference filter(s), and finally the imaging optics onto the photocathodes. Obstructions within the aperture of the far-range primary mirror, resulting from the secondary mirror, the near-range telescope, and the laser-beam outcoupling optics including their mountings and blocking about 28% of the telescope's surface area, were considered in the beam path. Actual substrate sizes, materials, and lens parameters were used. Because exact coating information is usually not provided by the suppliers of optical elements, either the explicit transmission and reflectivity information from the manufacturer was used or the coatings were realistically modeled.

Figure 2 shows overlap functions obtained from the ray-tracing simulations and resulting molecular-nitrogen (N_2) Raman signals for idealized atmospheric

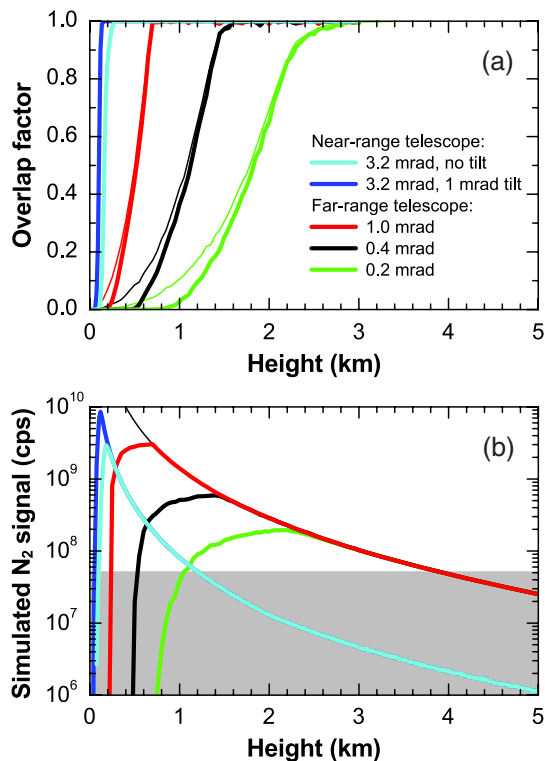


Fig. 2. Overlap functions and resulting N_2 signals in a pure molecular atmosphere simulated for near-range (blue) and far-range detection channels. The FOV of the far-range telescope is 0.2 (green), 0.4 (black), and 1.0 mrad (red). Thick and thin lines show the results including and neglecting shadow effects of obstructions within the telescope's aperture, respectively. An overall system efficiency of 0.5% is assumed. The gray-shaded area indicates signal intensities to which the photon-counting technique can be applied.

conditions (no particle extinction, night time). The overlap functions were calculated using 10,000 rays for each height range in steps of 50 and 15 m for the far and near ranges, respectively. The overlap functions for the far range are optimized such that complete overlap is reached at heights as low as possible without losing any signal at upper heights. The optimum overlap function is obtained when the field stop is placed 7.4 mm behind the telescope's focus. At this position the image of an object (i.e., the volume illuminated by the laser beam) at 5 km distance from the telescope is located. The overlap function for the near-range setup can be optimized by tilting the telescope against the laser beam by 0.5–1 mrad. In this way, complete overlap can be reached at distances of 150–200 m.

The idealized N_2 Raman signals in Fig. 2(b) have been calculated assuming a laser pulse energy of 500 mJ (as an upper limit) and an overall system efficiency of 0.5%. The gray-shaded area indicates signal intensities to which the photon-counting technique can be applied when dead-time effects are appropriately considered. When the signal strength is higher, the combination of analog and photon-counting detection is advisable. Otherwise, the signals have to be reduced to reasonable intensities

with the help of neutral-density filters. At daytime, background lighting adds to the signals. Then, a small FOV has to be chosen and the incomplete overlap can influence measurements up to heights of 2–3 km for the far-range setup (see green curves in Fig. 2). At night time, when a wider FOV can be applied, a complete overlap can be reached theoretically at about 1 km (see red curves in Fig. 2). Still heights between about 200 m and 2 km are best covered with the near-range setup. However, the signal dynamics is very high in this low height range. Therefore, one has to take care that detectors and data acquisition electronics show the required linear response. The system must be designed such that necessary adaptations of signal intensity to meet the requirements of the data acquisition (e.g., for “gluing” of analog and photon-counting signals [19]) are possible in dependence of the actual measurement situation. Therefore, almost all RAMSES detection channels are equipped with a set of neutral-density filters, implemented in a motorized control box (see Section 2.B.3).

2. Imaging

A known problem of PMTs is that the sensitivity of the photocathode may vary across its surface [20]. To avoid a range-dependent modulation of the lidar signal [21] by a shifting image of the light pulse propagating through the atmosphere, one can image the aperture of the telescope’s primary mirror on the photocathode. This concept was applied to the optical design of the RAMSES far-range polychromator unit (Fig. 3).

The elements of the imaging optics are shown in Fig. 3(a). A collimator consisting of two lenses with an effective focal length of 187.5 mm is placed 205 mm behind the field stop. Its position is optimized such that best collimation is reached on the path between the collimator and the objective where all beam splitters and filters are located. Figure 3(c) shows the angular distribution of rays from different heights in the collimated beam. The angle of incidence (AOI) with respect to a plane perpendicular to the optical axis is less than 0.9° in all cases. Typical acceptance angles of narrow-bandwidth interference filters are of the order 2° as the ZEMAX calculations show. Thus, by keeping the AOI below 1° for all measurement heights, a height-independent filter transmission is assured. The first real image of the telescope mirror occurs 194 mm behind the collimator. With the help of the objective–eyepiece ensemble in front of each PMT, a further image is created that is to be placed onto the photocathode. For the sake of experimental simplicity, the objectives were chosen to be equivalent to the collimator and the distance between objective and eyepiece to be the same for all channels. The eyepiece consists of a single lens with 50 mm focal length. The only parameter to be optimized for each channel was then the distance d_{opt} between the eyepiece and the photocathode on which the image had to be located. In dependence on the collimator–objective distance, which lies between 473 (channel A) and 1015 mm (channel E) (see Section 2.B.3), d_{opt} varies between 35.5 and 20 mm. The corresponding image sizes are between 5.4 and 2.9 mm, respectively,

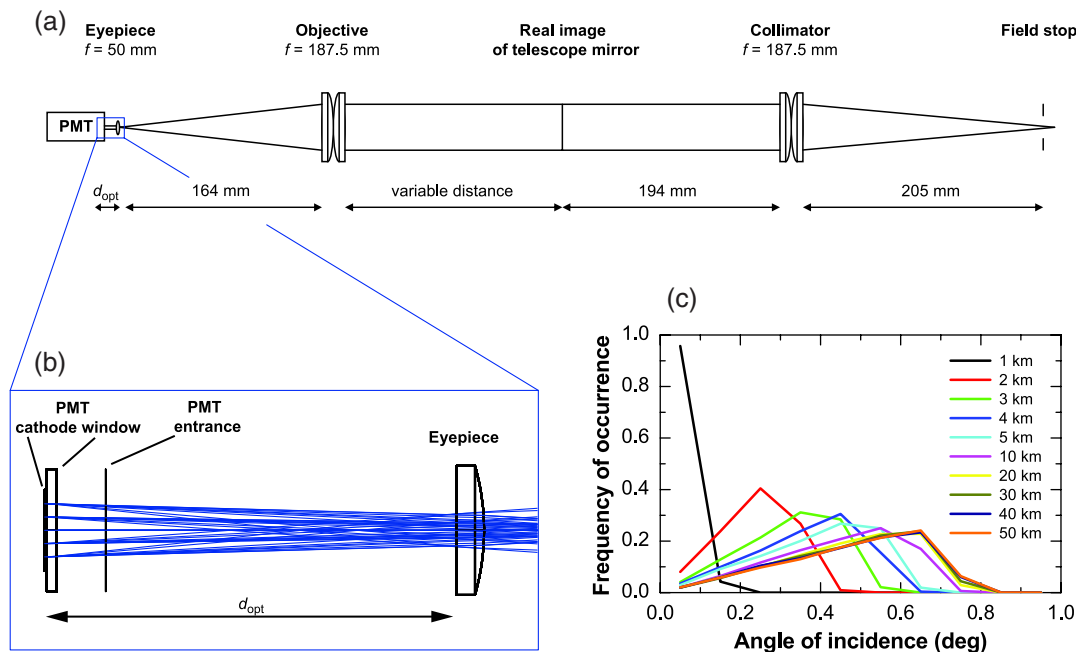


Fig. 3. Concept of optical imaging in the far-range polychromator unit. (a) Behind the field stop (right) the beam is collimated and passes the individual beam-separation optics of each channel. Afterwards, an objective–eyepiece setup in front of the PMT (left) produces an image of the telescope’s primary mirror. (b) Distance between the eyepiece and the PMT is optimized such that the image is formed exactly on the photocathode. (c) Angle-of-incidence distribution in the collimated beam for rays arriving from heights between 1 and 50 km.

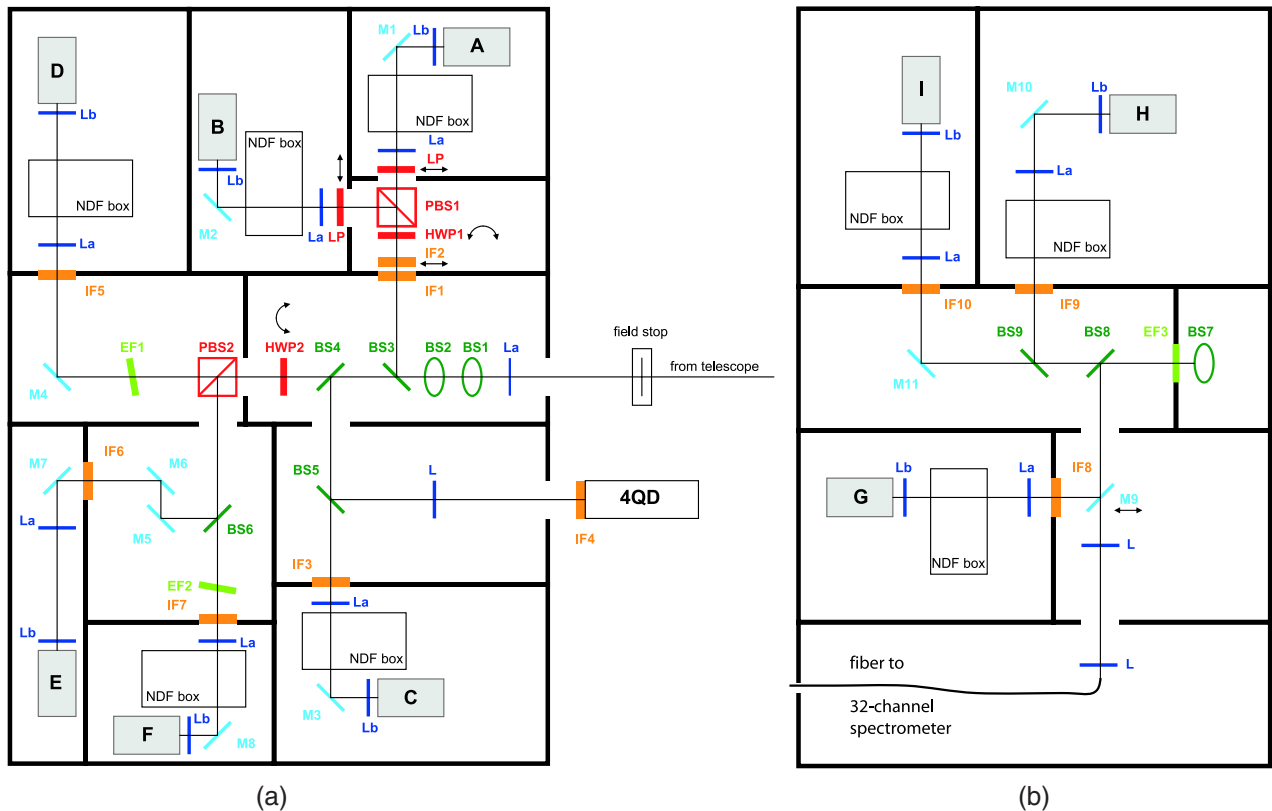


Fig. 4. Schematic view of the far-range polychromator unit with (a) six detection channels (A–F) in the lower level and (b) three detection channels (G–I) in the upper level. Colors indicate the function of the optical elements: beamsplitters (dark green, BS); interference filters (orange, IF); edge filters (light green, EF); mirrors (cyan, M); polarizing elements (red, PBS, polarizing beamsplitter; HWP, half-wave plate; LP, linear polarizer); lenses (blue, L, La, collimator/objective; Lb, eyepiece; see Fig. 3).

thus fitting well onto the photocathodes (8 mm diameter).

The PMTs of the near-range polychromator are illuminated directly by the collimated light beam. This approach requires the photocathodes to be relatively large (22 mm diameter). The optical path lengths are the same for all detection channels. For more information, see [13].

3. Polychromator Units

Figures 4 and 5 show schematic diagrams of the far-range and near-range polychromator units, respectively. Table 2 provides an overview of the 12 receiver channels with respect to measured signals, center wavelength, bandwidth, and peak transmission of the interference filters, as well as an estimate of the optical channel transmission at the center wavelengths. Channels A–I belong to the far-range polychromator, channels K–M to the near-range polychromator.

Customized interference filters listed in Table 2 as well as beamsplitters described below were manufactured by Barr Associates, Westford, Massachusetts. (now Materion Barr Precision Optics and Thin Film Coatings). Suppliers of other elements are explicitly mentioned in the text. The optical parameters of the filters and beamsplitters were selected such that

optimum signal-to-noise ratio and sufficient suppression of cross-talk from elastically scattered light are obtained in all Raman channels (D, F, G, H, I, K, L) under daytime and night-time conditions. The respective filter design requirements are well known from the literature and not discussed in detail here, see, e.g., [5,9,22].

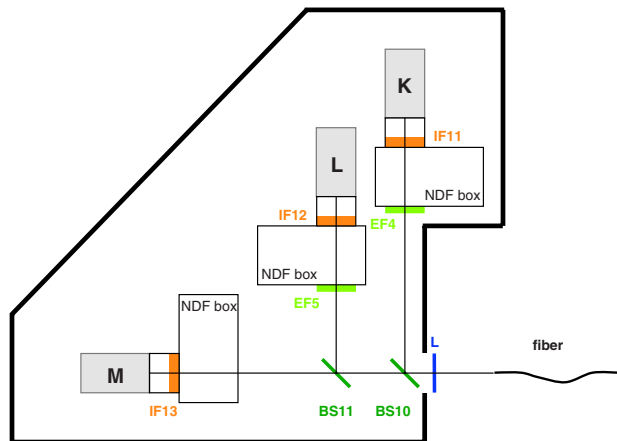


Fig. 5. Schematic view of the near-range polychromator unit with three detection channels (K–M). Colors indicate the function of the optical elements: beamsplitters (dark green, BS); interference filters (orange, IF); edge filters (light green, EF); lens (blue, L).

Table 2. Optical Characteristics of the RAMSES Receiver Channels^a

Channel	Signal	Filter No.	CWL, nm	Bandwidth, nm	Peak Filter Transmission, %	Optical Channel Efficiency at CWL, %
A	EL, cr	IF1/2	354.63/354.71	4.95/0.56	61.0/60.6	0.52
B	EL, co	IF1/2	354.63/354.71	4.95/0.56	61.0/60.6	0.46
C	EL, un	IF3	354.71	0.56	59.6	1.26
D	RR, cr	IF5	355.39	0.15	34.1	12.0
E	EL, co	IF6	354.64	1.98	62.0	20.6
F	RR, co	IF7	356.26	0.55	47.7	13.5
G	VR, H ₂ O	IF8	407.54	0.22	80.8	37.3
H	VR, N ₂	IF9	386.68	0.22	82.9	4.56
I	VR, N ₂	IF10	386.70	0.22	85.5	34.0
K	VR, H ₂ O	IF11	407.55	0.23	62.0	37.1
L	VR, N ₂	IF12	386.68	0.22	67.2	37.5
M	EL, un	IF13	354.64	1.95	61.0	33.7

^aChannels A–I belong to the far-range polychromator, channels K–M to the near-range polychromator. CWL—center wavelength, EL—elastic signal, RR—rotational Raman signal, VR—vibrational-rotational Raman signal, co—co-polarized component, cr—cross-polarized component, un—unpolarized signal. The optical channel efficiency is the estimated throughput from the atmosphere to the PMT photocathode, including the glass window, but not including the detection efficiency of PMT and data acquisition.

The schematic of the far-range polychromator is presented in Fig. 4. The unit is divided into two levels shown in Figs. 4(a) and 4(b), respectively. To isolate each detection channel of the receiver against ambient light and cross-talk from other channels, the two mechanical polychromator levels were milled out of solid blocks of tempered aluminium. Further, each detection channel is placed in an individual chamber (indicated by thick black lines in Fig. 4) equipped with the PMT, its imaging optics, and, in most cases, an assembly of motorized neutral-density filters (NDF) used to adjust the intensity level of the lidar signals (see Section 2.C). The entrance apertures of these chambers have mounting threads for optical elements, in most cases interference filters for optimum out-of-band blocking. All electric feed-throughs were realized with special wall-mounted connection jacks to avoid any stray light entering the chambers.

The first optical element behind the field stop is the lens collimator (La) as described in Section 2.B.2. The lower level of the polychromator [see Fig. 4(a)] contains six channels (channels A–F) detecting elastic-backscatter and pure rotational Raman signals <357 nm. In the upper level [see Fig. 4(b)], the three vibrational-rotational Raman channels (channels G–I) for the detection of water-vapor and N₂ signals are located. Dichroic beamsplitter BS1 with high reflectivity (>99%) for wavelengths >385 nm and high transmission (>95%) for wavelengths from 351 to 359 nm is applied to separate the light beams of the two levels. The reflected fraction is directed vertically toward the upper level, while the transmitted part remains in the lower level. Here, the following beamsplitter BS2, a fused-silica plate with antireflection coating and same geometrical properties as BS1, corrects for the geometrical beam displacement caused by BS1. Beamsplitters BS3–BS5 have identical coating. They are used to reflect about 6% of the light beam and transmit the remainder. The coating is designed such

that the reflectivity is nearly the same for light with parallel and perpendicular polarization with respect to the plane of incidence. With these beamsplitters, a small fraction of the lidar return signal is directed toward channels A–C for the detection of elastic backscattering and toward a four-quadrant detector (4QD, Licel) used for active beam stabilization (see Section 2.C). About 88% of the signal, however, is passed through toward channels D–F.

Channels A and B are dedicated to measurements of the linear depolarization ratio. Therefore, the elastic-backscatter signal is divided into a parallel and a perpendicular polarization component with respect to the plane of the optical table (the plane of polarization of the outgoing laser beam is parallel to the optical table). Because measurements of linear depolarization ratio require an adequate cross-talk suppression between the channels, the polarizing cube beamsplitter (PBS1, manufactured by Optarius, Malmesbury, United Kingdom) is followed by additional linear polarizers (LP, manufactured by Codixx, Barleben, Germany) so that an extinction ratio of better than 1:10,000 is guaranteed in both channels. A multiple-order half-wave plate HWP1 (VLOC, New Port Richey, Florida, mounted on an OWIS rotary-measuring stage) is implemented in front of PBS1 to make the polarization planes of transmitter and receiver coincide exactly. Cross-polarized light is detected in channel A and co-polarized light in channel B. HWP1 is also necessary for the calibration of the polarization channels after the method suggested by Alvarez *et al.* [23]. In channel C, an elastic-backscatter signal without polarization discrimination is detected. Thus the three-signal method after Reichardt *et al.* [24] can be applied alternatively.

Channels D and F represent the temperature measurement channels and detect pure rotational Raman signals. The beam separation applies a new principle that is detailed in Section 2.B.4. Channel E measures elastic backscattering (co-polarized component) from the upper atmosphere (>10 km)

and is equipped with a gated PMT to suppress signals from the troposphere. Therefore, this channel has no NDF box. Mirrors M5 and M6 are used to align the beam when BS6 is tilted to optimize the signal of channel F (see Section 2.B.4).

The upper level of the far-range polychromator contains the channels G–I for the detection of vibrational-rotational Raman signals. Two optical elements at the entrance of the upper level serve to minimize parasitic solar-background and laser light in the polychromator. First, BS7 reflects only light between 381 and 420 nm toward the detection channels; other wavelengths are transmitted with about 95% efficiency and subsequently blocked. Second, edge filter 3 (EF, model LP02-355RU, Semrock RazorEdge, Rochester, New York) with a suppression of $>10^5$ at 355 nm and a transmission $>95\%$ for wavelengths >358 nm is placed behind BS7 to prevent stray light from the laser and elastic-backscatter signals from entering the upper level. Together with the respective interference filters, a suppression of elastic-backscatter light in the Raman channels of $>10^{12}$ is reached (provided that no stray light bypasses the optical elements and enters the detectors).

BS8 is a dichroic beamsplitter with high reflectivity for wavelengths >391 nm, particularly at 407.5 nm (water-vapor Raman band), and high transmission at 386.7 nm (N_2 Raman signal). The water-vapor signal is detected in channel G. The N_2 Raman signal is further split by beamsplitter BS9 into a low-intensity signal in channel H and a high-intensity signal in channel I. The beamsplitter has a reflectivity of about 11% at 386.7 nm for both polarization components. Channel I is used for upper-atmosphere measurements. As in channel E a gated PMT is applied. Mirror M9 is mounted on a translation stage. If moved out of the light beam, not the water-vapor detection channel G is illuminated but a three-lens fiber coupler. This option is currently used for the implementation of a spectrometer to measure the Raman spectra not only of water vapor but also of liquid water and ice [25].

The setup of the near-range polychromator unit is outlined in Fig. 5. Essentially, its configuration with three detection channels for the measurement of total elastic backscattering and of Raman scattering from N_2 and water vapor (see Table 2, channels K–M) has not changed since RAMSES was commissioned in the year 2005 [13]. A lens doublet with an effective focal length of 62.5 mm at the entrance collimates the light coming from the fiber (see Section 2.A). The collimated beam with a diameter of <20 mm is split by the dichroic beamsplitters BS10 and BS11 and, after passing the respective interference filters IF11–IF13, directly hits the PMT photocathodes without focusing. Edge filters EF4 and EF5 are implemented in the two Raman channels to further enhance the suppression of elastically scattered light. As in the far-range polychromator, neutral-density filters assembled in NDF boxes allow for an adaption of the signal strengths.

4. Implementation of the Rotational-Raman Temperature Method

The optical design of the temperature measurement setup exploits the fact that the rotational Raman lines possess a high linear depolarization ratio of 0.75. So by splitting the lidar return from the atmosphere into its co-polarized and cross-polarized components (with respect to the laser emission), one can obtain with similar signal strength the two signals needed for the temperature measurements, i.e., the low- and the high-quantum-number rotational Raman signals S_L^{RR} and S_H^{RR} , respectively. S_L^{RR} is spectrally closer to the laser wavelength, so it is particularly challenging to minimize the effects of elastic-light leakage here. One measure that helps in this context is to assign the cross-polarized signal component to S_L^{RR} because here the ratio of inelastically to elastically backscattered light is always higher than in co-polarization, particularly in water clouds and cirrus clouds with horizontally aligned ice particles. The co-polarized signal component is assigned to S_H^{RR} . Another advantage of using the polarization state for signal separation is that since S_L^{RR} and S_H^{RR} are then either parallel- or perpendicular-polarized with respect to the planes of incidence of the optical elements, one can use tilted edge filters efficiently to further improve shielding from elastic backscattering (the position of the filter edge depends on both the AOI and the polarization vector). Because only long-pass edge filters are readily available that show the required edge steepness, one has to extract the rotational Raman signals from the Stokes wing of the spectrum.

In our setup, half-wave plate HWP2 behind BS4 serves to rotate the polarization vector of the incoming light so that its co-polarized component (with respect to the laser emission) is normal to the plane of incidence of polarizing beamsplitting cube PBS2 and thus reflected at its dielectric coating while the cross-polarized component is transmitted [Fig. 4(a)]. This is done to exploit the high extinction ratio ($>1000:1$) of the polarizer in transmission to optimally suppress elastic-backscatter light in S_L^{RR} (detected in channel D). Next come edge filter EF1 (AOI = 11.2° , Semrock RazorEdge LP02-355RU), a bending mirror, and interference filter IF5 (AOI = 0°) sealing the aperture to the detector chamber. The S_H^{RR} optical branch is similar, except that an additional beamsplitter (BS6, AOI = 44.7° , Barr) is inserted to reflect most of the co-polarized elastic light, which is detected in channel E and used for aerosol and integration-method temperature measurements in the stratosphere. EF2 (AOI = 13.0° , Semrock RazorEdge LP02-355RU) further reduces the elastic-light contributions to the S_H^{RR} signal before full out-of-band blocking is accomplished by IF7 (AOI = 0°) in front of detector chamber F.

Figure 6 illustrates the optical transmission curves of the channel-D and channel-F beamsplitter assemblies (including PBS2, EF1, EF2, and BS6) and of the interference filters. Actual measurements of

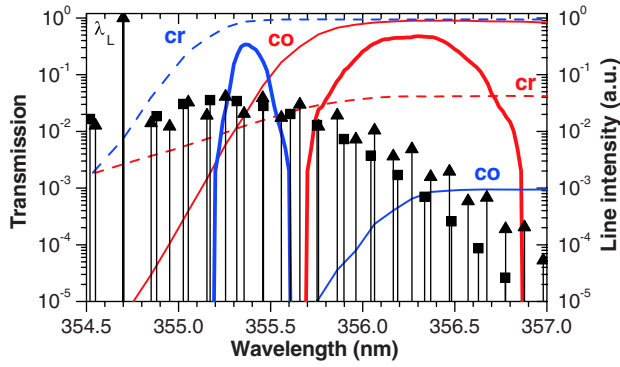


Fig. 6. Transmission of the interference filters (thick curves) and of the beamsplitter assemblies [thin curves, cross-polarized (cr) and co-polarized (co) components with respect to the laser polarization vector] of the low-quantum-number rotational Raman channel (blue) and the high-quantum-number rotational Raman channel (red) as a function of wavelength. The rotational Raman spectra of molecular nitrogen (▲) and molecular oxygen (■) are shown for comparison. The laser line is also indicated (λ_L).

these optical elements have been used for this compilation except in two cases. First, the transmission curves that were delivered together with the interference filters showed a background noise of about 0.1%, which is why theoretical transmission values were substituted for readings below this level. Second, typical transmission data provided by the manufacturer were used for EF. The edge positions of EF1, EF2, and BS6 were determined from the respective incidence angles and effective refractive indices; in the case of EF2 the calculated edge position was confirmed experimentally. According to these data, the beamsplitter assemblies reject the co-polarized elastic-backscatter signal efficiently with transmission $<3 \times 10^{-9}$ and $<5 \times 10^{-6}$ in channels D and F, respectively. Thus in combination with the interference filters (optical depth of about 8 at the laser wavelength, according to the manufacturer), signals S_L^{RR} and S_H^{RR} can be considered as unaffected by this light component. Beamsplitter transmission of the cross-polarized elastic-backscatter signal is higher in both channels (0.003–0.008), which leaves the temperature measurement more vulnerable to cloud-induced errors, especially in cirrus clouds with high backscatter and depolarization ratios. However, the routine observations show that the temperature polychromator performs well in ice clouds except for the optically very thick. Figure 7 displays, as an example, a temperature measurement in a cirrus cloud with a maximum backscatter ratio of 60. No cloud-correction scheme was applied. Evidently, the cloud does not interfere with the temperature measurement.

Figure 8 shows the optical transmission of the S_L^{RR} and S_H^{RR} detection channels as a function of atmospheric temperature. The temperature sensitivity of S_H^{RR} is pronounced with a slope of, on average, 0.48%/K. S_L^{RR} exhibits the expected inverse behavior and is, in absolute terms, about half as large ($-0.21\%/K$). Nevertheless, this value is quite

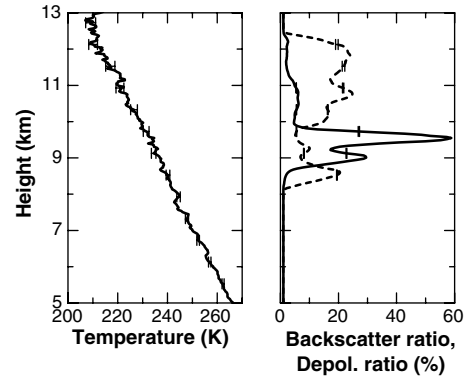


Fig. 7. Rotational-Raman temperature measurement in the presence of a cirrus cloud (backscatter ratio, solid curve; volume depolarization ratio, dashed curve) around 00:20 UTC on 6 June 2010. 1200 s of lidar data are integrated. The resolution of the raw data is 30 m, profiles are smoothed with a sliding-average length of five height bins. Bars indicate statistical errors.

satisfactory because it is a challenging task to design a temperature polychromator with the low-quantum-number rotational Raman channel bandwidth as close as possible to the laser wavelength, which is necessary for a high temperature sensitivity while avoiding optical leakage from same.

If R is the ratio of the S_H^{RR} and S_L^{RR} signals in photon counts per height bin,

$$R = S_H^{RR} / S_L^{RR}, \quad (1)$$

then Gaussian error propagation yields for the absolute statistical measurement error of temperature T :

$$\Delta T = \frac{dT}{dR} R \sqrt{\frac{1}{S_L^{RR}} + \frac{1}{S_H^{RR}}}. \quad (2)$$

Poisson signal statistics are assumed ($\Delta N = \sqrt{N}$). Function RdT/dR is shown in Fig. 8. It was calculated with the polychromator data of Fig. 6 and with

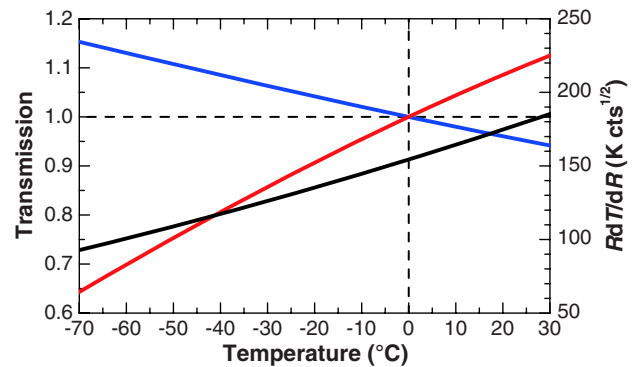


Fig. 8. Temperature dependence of the transmission of the low-quantum-number rotational Raman channel (blue curve), the high-quantum-number rotational Raman channel (red curve), and term RdT/dR of Eq. (2) defining the statistical measurement error (black curve). The transmission curves are normalized to their values at 0°C.

modeled rotational-Raman spectra. The function's increase with ambient temperature means that for a given temperature error one has to collect more signal counts at warmer than at colder temperatures. As an example, at 0°C, $N = 40,000$ is necessary for a temperature error of ± 1 K (equal signal strengths assumed). Calibration of the rotational-Raman temperature measurements is described in Section 3.

C. Systems Control and Automated Operation

Autonomous operation is the key requirement for the RAMSES design. As the result, the RAMSES control system emulates the performance of a human operator with all his senses and experience. Figure 9 provides an overview of the internal and external communication links. The operational tasks are distributed between two industrial-grade computers, the measurement-execution computer (MEC) and the systems-control computer (SCC). The MEC is used for controlling laser operation, the acquisition electronics with its photon-counting units and analog-digital converters and for active steering of

the motorized lidar components. The SCC computer acts as a central control unit for the complete remote-sensing system.

A number of lidar components are actively controlled via the MEC. Most important is the automatic beam-alignment system based on a 4QD. A closed-loop software control evaluates the 4QD signals and provides corrective signals to two micro-actuators, which steer one of the transmitter mirrors in order to keep laser beam and receiver optical axis aligned. Further interfaces exist to select the lidar's FOV via the motorized iris, to drive the neutral-density filters, to run the polarization calibration procedure (HWP1, LP, IF2), to optimize the performance of the rotational Raman measurements (HWP2), and to activate the 32-channel water spectrometer (M9).

The SCC supervises a variety of external probes, e.g., brightness and precipitation sensors, and gathers meteorological data and cloud base-height information from a local laser ceilometer. In this way, system operation can be adapted to actual observation conditions. Autonomous operation demands a

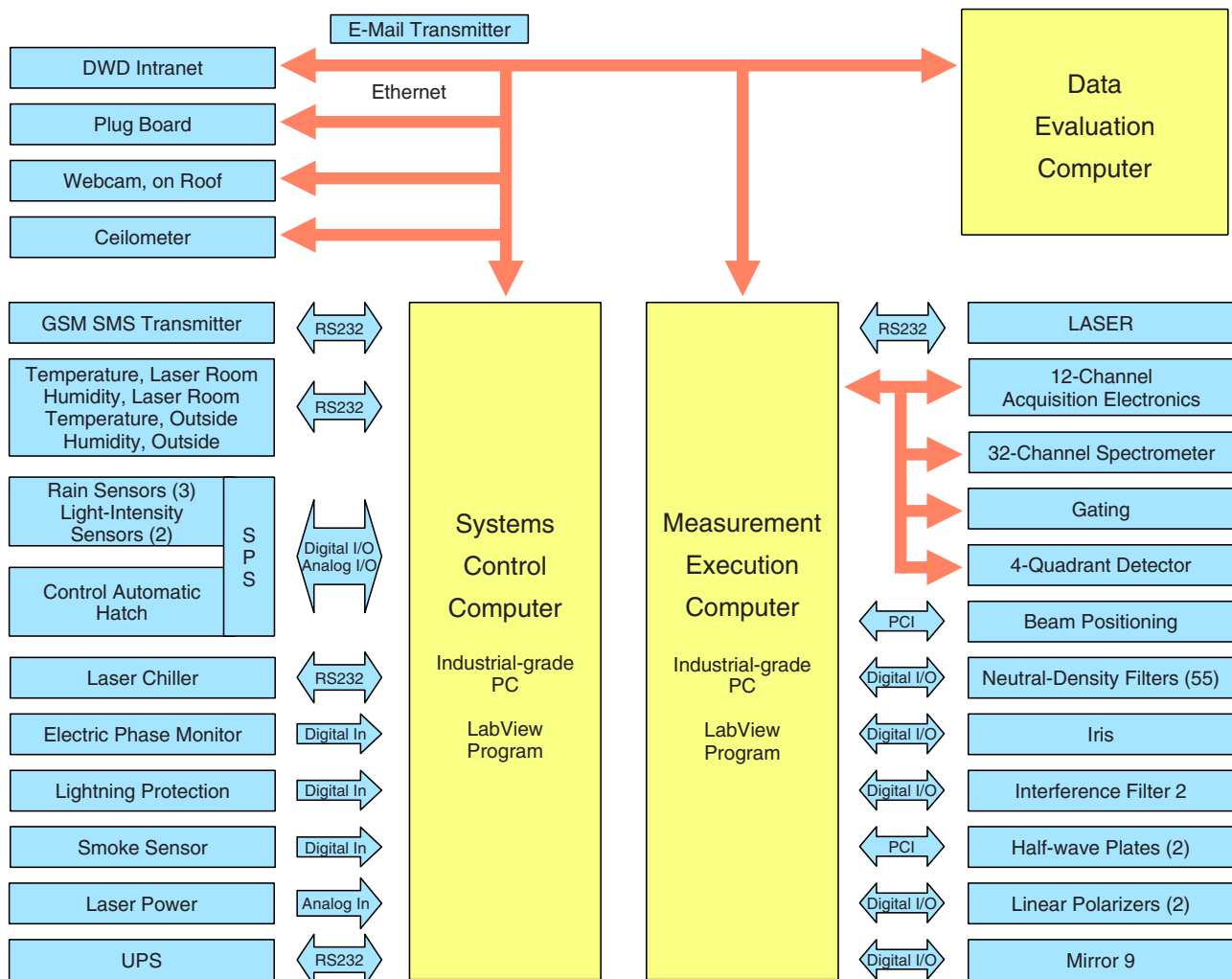


Fig. 9. Overview of the RAMSES control system. A network of three computers controls data acquisition and measurement setup (measurement-execution computer, MEC), environmental conditions and safe operation (systems-control computer, SCC), and NRT data evaluation (data-evaluation computer, DEC).

number of safety features to ensure system reliability during unfavorable weather or other potentially dangerous operating conditions. A sensor suite covers lightning protection, smoke detectors, temperature and humidity sensors at different places inside the container as well as a monitor to survey the power of the laser pulses. Additional sensors control the status of the hydraulic hatch, the UPS, performance of the data-acquisition system, the laser chiller, etc. All data are grouped according to a priority list in order to characterize the overall performance status of the RAMSES system. In case of a malfunction and depending on its cause and priority level, the SCC software initiates appropriate actions. Low-priority events lead to a temporary stop of the measurements, followed by an automatic restart after a predefined time period. Errors with higher priority result in a lidar shutdown, and alerts are distributed to RAMSES personnel via SMS. All subsystems respond to an automatic shutdown such that a hazardous system status is avoided.

The control software of RAMSES (housekeeping as well as data acquisition) is based on National Instruments LabVIEW, Version 9. The actual system status and the current lidar raw data are displayed on computer screens. Alternatively to autonomous operation, a graphical user interface allows for manual interactive systems control, i.e., modification of all system parameters and remote control of the laser and the receiver electronics. Some RAMSES subsystems can be operated in "service mode" for selective performance analysis, e.g., the laser.

The lidar raw signals are stored in NetCDF format on a local hard disk. The NetCDF files are created for each data-acquisition time step (usually 30 s). Although this setup requires more disk space than a single accumulative NetCDF file would, it is a very robust solution to avoid data loss due to file damages incurred by simultaneous file access from different users. Further, this setup allows for immediate transfer of raw data to the DEC for near-real-time analysis.

3. Automated Lidar Data Analyzer

The main task of the automated lidar data analyzer (ALDA) [26] is to provide the local 'Lindenberger Säule' (LS) database with RAMSES measurement products on a fully autonomous basis so that they can be disseminated to DWD and external users in near real time (NRT), e.g., for the assimilation in numerical weather prediction models. Input data to ALDA are the RAMSES raw signals and data from the operational radiosondes that are launched at Lindenberg at 00, 06, 12, and 18 UTC. The sounding data are available from the LS database (Oracle) about 1 to 1.5 h after a sonde was started. Currently, ALDA products are profiles of water-vapor-to-dry-air mixing ratio (MR), relative humidity, temperature (with rotational Raman technique), particle backscatter ratio, particle backscatter coefficient, particle

extinction coefficient, and particle extinction-to-backscatter (lidar) ratio.

The ALDA software works as a continuously running daemon process. A timer starts new analysis threads usually every 15 min. Those threads actively check whether new raw signals have been transferred from the MEC to the DEC or whether new radiosonde data are available from the LS database. If so, new raw signals or sonde data, respectively, are imported and a data processing chain is started. All products are calculated and visualized independently of each other. When the analysis of a complete measurement is finished, all relevant data and information are stored into an archive file.

ALDA can be operated in different modes. The *online mode* is designed for the autonomous analysis of lidar signals during an ongoing measurement and visualization of the current products in NRT. The *view mode* allows visualization of any already existing ALDA product in terms of profiles or time-series plots. It can also be used for a manual quality control of the autonomously generated products. The *archive mode* is designed to manage the backup and to restore processes of measurements. The *science mode* allows for interactive re-analysis of measurements with, e.g., manual inspection and quality control of raw signals, individual selection of time periods, or manual optimization of data analysis parameters. In *administration mode* the user can visualize and manage the RAMSES calibration constants. All parameters of the lidar data analysis can be optimized with ALDA's *graphical user interface*. The user can select which products are to be derived and which corrections are to be applied to the raw signals. Integration times and smooth intervals as well as quality control parameters can be specified individually for all products. It is possible to apply different parameter sets to daytime and night-time signals. Those options and parameters have to be defined once according to the hardware setup of the lidar and the user requirements, e.g., concerning accuracies. Then, these parameter sets remain unchanged; the autonomous data analysis is performed without any user interaction.

Upon import, RAMSES raw data are preprocessed by ALDA as follows. RAMSES signals (Licel acquisition system) are corrected for pulse pileup as nonpolarizable signals according to [27]. The height shift between the analog signals and the corresponding photon-counting signals has to be corrected before signal gluing is performed as described in [19]. The background value is calculated at the far end of the signals and subtracted. Raw signals are temporally averaged with integration periods between 30 s and 2 h. Rayleigh scattering is calculated from temperature and pressure profiles from a radiosonde observation using the formulas given in [28] and [29]. The data of the latest available radiosonde or the radiosonde that is closest in time to the lidar signals are used in *online mode* or *science mode*, respectively. The lidar signals are corrected for the dependence of

the Raman cross-section on ambient temperature [27] (except S_L^{RR} and S_H^{RR} when used for rotational-Raman temperature measurements). Vertical smoothing is realized in terms of a sliding average for all products, except extinction where it is constituted by the length of the fit window. For each signal, the user can define up to five smoothing intervals with variable boundaries and smoothing lengths between 7.5 and 1507.5 m. The signals are corrected for incomplete overlap.

After preprocessing, the products are calculated from the near-range and far-range signals separately before a composite product profile is formed. Statistical errors are obtained from the Poisson errors of the raw signals following Gauss' error propagation law. The ensuing automated quality control flags profile ranges where errors are larger than user-defined thresholds or where values are out of the physically meaningful range by more than the doubled value of their uncertainty. Finally, product profiles are stored in NetCDF format.

For NRT data analysis of humidity, temperature, and particle backscatter products, ALDA uses calibration constants that are averages of calibration data sets from previous measurements. When a radiosounding profile becomes available during the running measurement, a new set of calibration data is calculated automatically. For reasons of consistency, this set is not included in the ongoing data analysis but only available to following RAMSES measurements. This strategy results in a large number of calibration data sets that allows for the identification of trends or outliers using the *administration mode*. The neutral-density filter configuration may change from measurement to measurement and even during an ongoing measurement, e.g., by the hand of the operator or automatically on day-night transition. Because the calibration constants have to be applicable to other measurements than the one during which they were determined, ALDA determines and stores generalized calibration constants from which the impact of the neutral-density filters is removed. The required transmission values of the neutral-density filters have been obtained with a Varian Cary 400 spectrophotometer, the measurement uncertainty is estimated to be better than 1% for all filters.

The calibration of the water-vapor-to-dry-air MR m_{H_2O} is performed with those lidar signals that were measured exactly at the time the sonde passed through the user-defined calibration height range. Height bins with ambient temperatures below a specified threshold (typically -40°C) are excluded to avoid systematic calibration errors due to any radiosonde dry bias at cold temperatures. The calibration factor of a specific measurement is the mean value of the ratio of m_{H_2O} measured by sonde and the ratio of the water-vapor Raman signal to the molecular-nitrogen Raman signal over the calibration height interval. The profile of the relative humidity is calculated from the water-vapor-to-dry-air MR profile and,

currently, from sonde temperature data. The latter are obtained by interpolating the temperature profiles of radiosoundings before and after the measurement. The larger the time difference between the lidar measurement and a sounding, the larger are the temperature errors and the resulting uncertainties in relative humidity. Preferably, a temperature profile would be used for the computations that was measured along with m_{H_2O} . For this reason, it is planned to modify ALDA and exploit the RAMSES rotational-Raman temperature profiles in future observations.

The calibration procedure for rotational-Raman temperatures makes use of the signal-ratio profile R of Eq. (1). R is normalized with the transmission values of the neutral-density filters in both channels. The calibration function

$$R(T) = \exp(a/T^2 + b/T + c), \quad (3)$$

with a , b , and c the fit parameters, is chosen because this ansatz has been shown to be superior to other functions [30]. Solving Eq. (3) yields two solutions of which the physically meaningful one is not known a priori. So to determine the optimum solution, temperature profiles are reconstructed for both and compared with the sonde profile. The one with the better agreement is then selected.

The backscatter ratio is the calibrated ratio of the elastically backscattered signal to the vibrational-rotational N_2 Raman signal. Because the calibration is performed over a height interval of negligible particle scattering in the free troposphere or lower stratosphere where near-range signals are noisy, the far-range backscatter-ratio profile is calibrated first. The calibration factor for the near-range backscatter ratio is subsequently determined by minimizing differences between near-range and far-range backscatter-ratio profiles at lower heights. Particle backscatter coefficients are derived from the backscatter ratios by subtracting Rayleigh backscattering. Extinction coefficients are calculated using the method described in [31]. Profiles of particle lidar ratio are computed by forming the ratio of the profiles of particle extinction coefficient and particle backscatter coefficient.

4. System Performance

A. Signal Shape and Intensity

In the following, a measurement during a clear night is investigated in more detail in order to evaluate the system performance in view of the design concept. The measurement was performed from 22:54 to 23:14 UTC on 24 May 2011, in coincidence with the regular night-time radiosonde ascent at Lindenberg (launch time at 22:54 UTC). Figure 10 shows the signals (red lines) obtained in the far-range water-vapor channel (channel G, upper left), the far-range and the upper-atmosphere N_2 Raman channels (channels H and I, respectively, upper

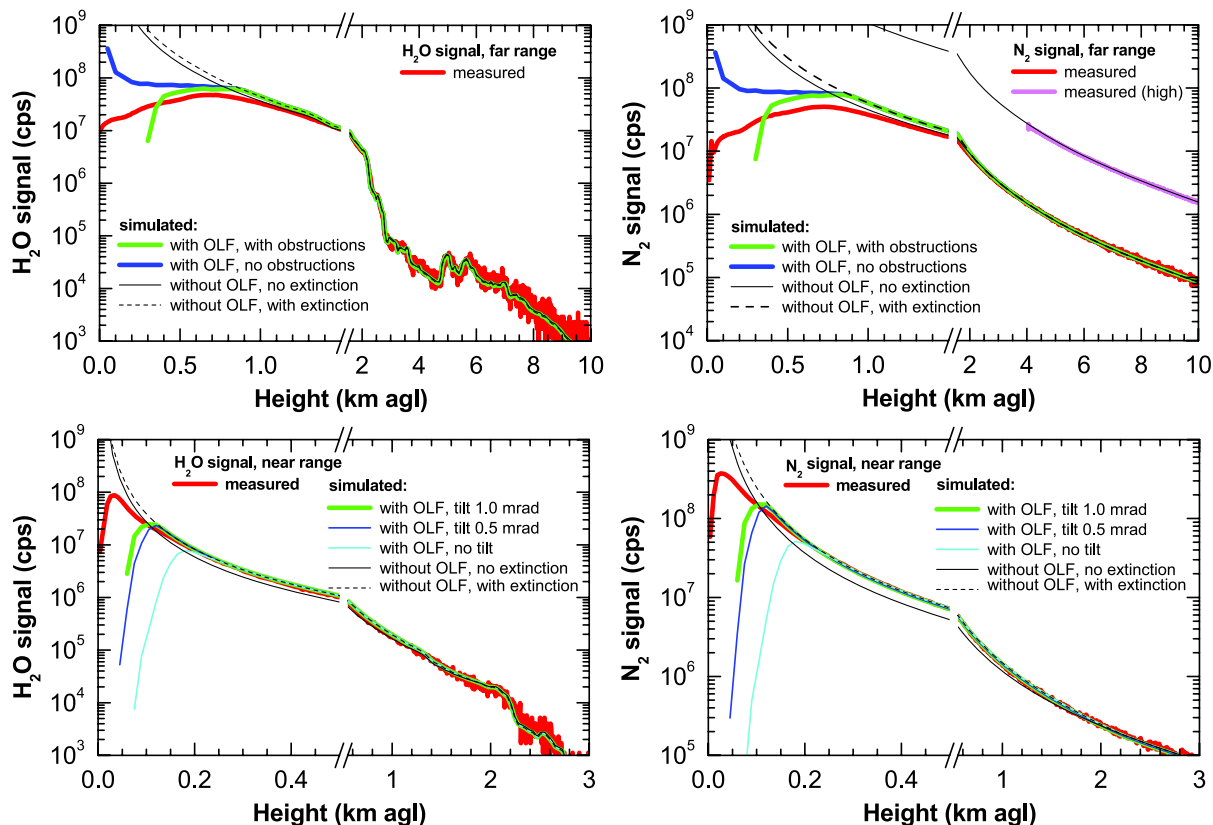


Fig. 10. Comparison of measured and simulated water-vapor (left) and molecular-nitrogen Raman signals (right) in the far-range (upper) and near-range channels (lower). The measurement was performed from 22:54 to 23:14 UTC on 24 May 2011. The simulations are based on water-vapor, temperature, and pressure profiles measured with a radiosonde launched at the lidar site at 22:54 UTC on 24 May 2011. The FOV of the far-range telescope was 0.75 mrad. Details are explained in the text. OLF, overlap function; agl, above ground level.

right), the near-range water-vapor channel (channel K, lower left), and the near-range N₂ Raman channel (channel L, lower right).

From the high-resolution radiosonde data, respective water-vapor and N₂ Raman signals were modeled with the end-to-end lidar simulator of the Leibniz Institute for Tropospheric Research in Leipzig, Germany [32]. Simulations were performed for both a pure molecular atmosphere (no aerosol extinction) and for an atmosphere with a constant aerosol extinction of 0.1 km⁻¹ between ground and 2.2 km height, i.e., an aerosol optical depth (AOD) of 0.22. This value was estimated from sun-photometry measurements at Lindenberg, which showed an AOD of 0.25 at 368 nm in the evening of 24 May 2011 (around 18 UTC) and of 0.12 in the morning of 25 May 2011 (around 4 UTC). According to the lidar measurements (e.g., backscatter-ratio profile), the aerosol was confined to the boundary layer, reaching up to 2.2 km (also indicated by the water-vapor signal in Fig. 10). Finally, the overlap functions as discussed in Sec. 2.B.1 were included in the modeled lidar signals as well.

The simulated signals were fit to the measured signals in the height range of 4–6 km and 300–500 m for the far and the near range, respectively. In general, excellent agreement between simulated and measured signals is found for the far-range signals

above 2 km and for the near-range signal above 200 m, i.e., no major problems concerning setup, adjustment, and performance of the system are encountered here. Below these heights, the overlap effect determines the actual signal shape. The signal maxima of the far-range signals occur at about 700–800 m height, which is in agreement with the simulation that takes into account an overlap function for a FOV of 0.75 mrad as used for this observation. But while a complete overlap is expected at about 1 km height from the simulation, measured and simulated signals only converge at about 2 km height. This behavior is often observed in measurements and, as the simulations show, can be caused by small imperfections of the lidar instrument, e.g., a higher laser-beam divergence than expected, an imperfect (non-Gaussian) beam shape, or errors in the positioning of the field stop.

The far-range signals below about 400 m height show a higher intensity than expected when considering all obstructions in the telescope aperture (see green curves in upper panels of Fig. 10). However, one should keep in mind that the obstructions are only very roughly estimated in the calculation of the overlap function by using circular and rectangular shapes. In this context it is instructive to examine the model results obtained without any obstructions (see blue curves in upper panels of Fig. 10).

Evidently, obstructions influence the shape of the overlap function below 500 m considerably. Moreover, the same effects that are probably the cause of the lack of signal between 1 and 2 km (gradual increase of the overlap function) can also lead to higher signals than expected at lower heights. Finally, stray light (multiply scattered light) from near distances after laser pulse emission may also contribute to the signals in the first few hundred meters.

As stated before, the measured near-range signals follow the simulations closely above 200 m (see lower panels of Fig. 10). Below, the overlap effect is visible but the signal maximum appears at much lower heights than expected. This behavior cannot be explained with a tilt of the telescope against the laser beam greater than 1 mrad (the maximum value presented in Fig. 10) or with optical misalignments, because these would lead to a loss of signal above 1 km, which is not observed. So probably here, too, signal contributions from short distances disregarded in the modeling effort may offer an explanation.

Finally, we estimate the overall system efficiency that we define as the constant of proportionality of the measured to the modeled signal. Simulations were performed for the laser energy of 350 mJ per pulse at that time and the actually available telescope area under consideration of obstructions. For the far-range water-vapor channel (channel G) and the upper-atmosphere N₂ Raman (channel I), in which no neutral-density filters were included, we obtained an overall system efficiency of 1.8% and 0.9%, respectively. Considering the theoretically calculated optical receiver efficiencies of 37% and 34% for the two channels (see Table 2) and assuming approximate values of the PMT quantum efficiency of 20% and of the data acquisition efficiency of 75% (due to low-pulse discrimination), we could expect a maximum theoretical system efficiency of 5.6% and 5.1%, respectively. Obviously, transmission losses reduce the system efficiency by a factor of 3–6. The losses may have manifold reasons. In the emitting and receiving optics the light passes about 35–45 optical surfaces (depending on channel) where scattering and absorption processes may occur. Aging of coatings and radiation-induced transmission losses of optical substrates (e.g., the Borofloat 33 glass window) are known to play a role in particular in the ultraviolet region. Also, losses due to electronics settings or aging of the PMTs cannot be ruled out.

B. Long-Term Optical Stability

Initially it was intended that the RAMSES water-vapor measurements were only calibrated with a radiosonde after changes to the experimental setup, and that the established calibration constant was to be used for all subsequent observations. However, sporadic cross checks indicated an apparent wetting of the lidar moisture profiles over time, which led to further investigations on the issue. The analysis of about 120 simultaneous lidar and radiosonde measurements taken in 2008–2009 corroborated the

initial results (Fig. 11). With a value of about $-(7.3 \pm 1.3)\%/year$, the decrease of the calibration constants of both the near- and the far-range water-vapor MR was substantial. The effect was not correlated with ambient conditions, so it was probably caused by a slow degradation of some optical elements, or the detectors. Similarly, the calibration constant of the far-range backscatter ratio decreased over time, albeit at the slower rate of $-(2.9 \pm 0.7)\%/year$. Only in the case of the near-range backscatter ratio the change was insignificant. As a consequence of these findings, RAMSES and radiosonde water-vapor measurements are now compared on a regular basis, and the calibration constants are updated if necessary.

C. Operation

After solving some initial problems, the operational software for systems control and automated measurement has been working stably and reliably. Unfortunately, this has not always been the case for the technical infrastructure. Most notably the air-conditioning proved to be insufficient to shield the RAMSES instrument from the environment completely, which may result in data losses due to lidar misalignment, especially for narrow FOVs in summer. Further, laser failures resulted in prolonged down times, mostly due to material fatigue of the pumping chambers and, in the early years of operation, due to chiller and remote-control issues. These technical problems but also the expansion of the receivers (e.g., installation of the new far-range polychromator in 2009 and the water spectrometer in 2011) and the at times unfavorable weather conditions reduced the number of measurement days to 100–180 per year in the 2006–2011 time frame.

5. Measurements

A. Multiday Observation

The measurement of 2–5 September 2011 is discussed to demonstrate the capabilities of the RAMSES instrument. Figure 12 displays false-color images of water vapor, backscatter coefficient, and

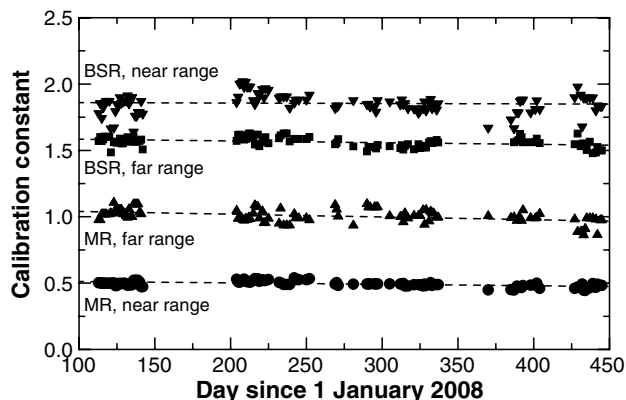


Fig. 11. Calibration constants of near- and far-range water-vapor MR and backscatter ratio (BSR) profiles over time. The results of linear fits to the data sets are also shown (dashed curves).

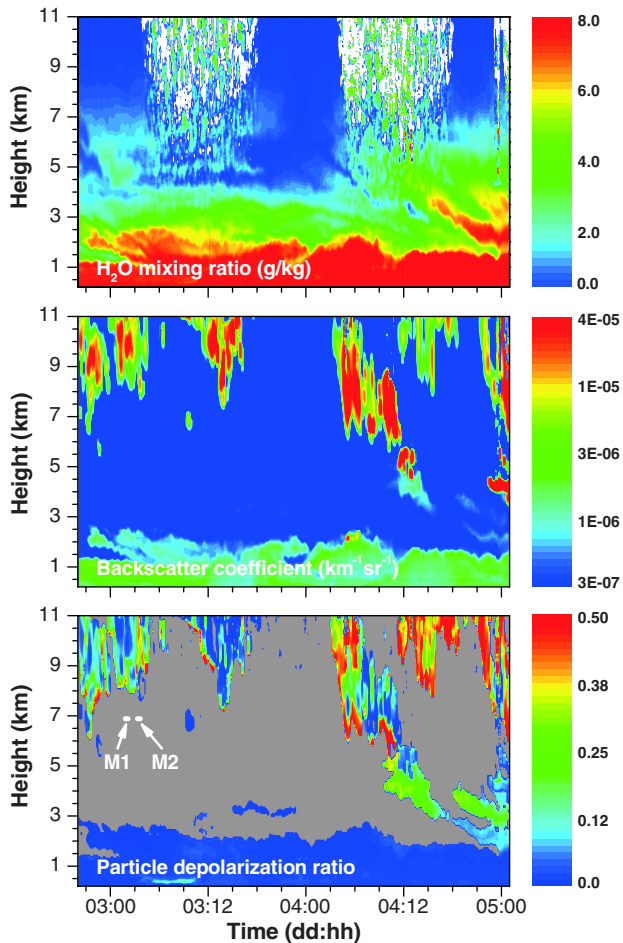


Fig. 12. Temporal evolution of water-vapor MR, particle backscatter coefficient, and particle depolarization ratio as measured with RAMSES on 2–5 September 2011, starting at 20:00 UTC. For each profile, 1200 s of lidar data are integrated; the calculation step width is 120 s. The resolution of the raw data is 60 m, signal profiles are smoothed with a sliding-average length of 3, 5, 7, 9, and 11 height bins from 1–2.5, 2.5–5, 5–7, 7–9, and 9–11 km, respectively. M1 and M2 indicate measurement segments that are presented in Fig. 15 in more detail.

particle depolarization ratio as an overview. The active overlap stabilization was turned on, and the FOV of the far-range receiver was set at 0.37 mrad for this measurement. Water-vapor profiling becomes feasible during daytime only with a narrow FOV, so one is restricted to using the far-range lidar signals for this purpose and need to compensate for the overlap functions of the far-range water-vapor and N_2 Raman signals at heights below 1 km. For this, overlap functions are first determined for each of the three nights (when near-range signals are available) by forming the ratios of the corresponding far-range and near-range signals and normalizing them at altitudes at which the overlap of the far-field signal can be assumed to be complete. Next, the individual overlap functions are averaged to obtain the mean overlap functions of both signals. Finally, the mean overlap functions are applied to the lidar data.

RAMSES daytime water-vapor measurements further require neutral-density filters in the Raman channels in order to avoid signal nonlinearities induced by the solar background. Filters with a transmission of 0.703 and 0.303 were therefore inserted in the far-range water-vapor and the N_2 Raman channel, respectively, which is sufficient for early September. The water-vapor calibration constant used is the average of all nine constants determined from the comparison of the RAMSES with the six-hourly radiosonde measurements between 3 September, 00:00 UTC, and 5 September, 00:00 UTC. The uncertainty of the mean calibration constant is 3%.

The measurement range of water-vapor MR exhibits a pronounced diurnal cycle due to background light, with values of around 5 km during the day and >11 km at night-time (Fig. 12). During most of the measurement period a translucent cirrus cloud was present, but in-cloud signal attenuation plays only a minor role in the reduction of the measurement range in this example, noteworthily only near the end of the observation. An interesting feature of the cirrus clouds is the high variability in particle backscatter coefficient and particle depolarization ratio, which is caused, at least in part, by fluctuating degrees of orientational freedom of the ice particles, to which the vertically-pointing RAMSES is sensitive. This effect is described in more detail when the cloud profiles of measurement segments M1 and M2 (indicated in the bottom panel of Fig. 12) are presented, but first the water-vapor performance of RAMSES is discussed.

Figure 13 compares the water-vapor profiles measured with RAMSES and the concurrent midnight Lindenberg routine radiosondes (RS92, Vaisala Oyj, Helsinki, Finland). For each comparison, 20 min of lidar raw data were integrated. The profiles show satisfactory agreement. Clouds were present in the first and the third night, but did not interfere with the water-vapor measurements directly because of the extreme rejection of elastically backscattered light by the edge filters and the interference filters. Still, clouds affect the measurements indirectly by signal extinction which reduces the measurement range. Under cloud-free conditions during the second night, the profile top height is 13–14 km. Note that the lidar measurements were performed with neutral-density filters inserted in the two Raman channels, which of course reduces the lidar performance in night-time measurements. In autumn 2011 the measurement software was therefore modified so that now RAMSES is always operated with an optimum set of system parameters (including neutral-density filters and field of view) depending on the background light level.

Fluorescence in the lidar receiver has been shown to impede water-vapor measurements in the upper troposphere and lower stratosphere in both fiber- and nonfiber-coupled lidar systems [8,33]. RAMSES measurements are regularly compared with humidity

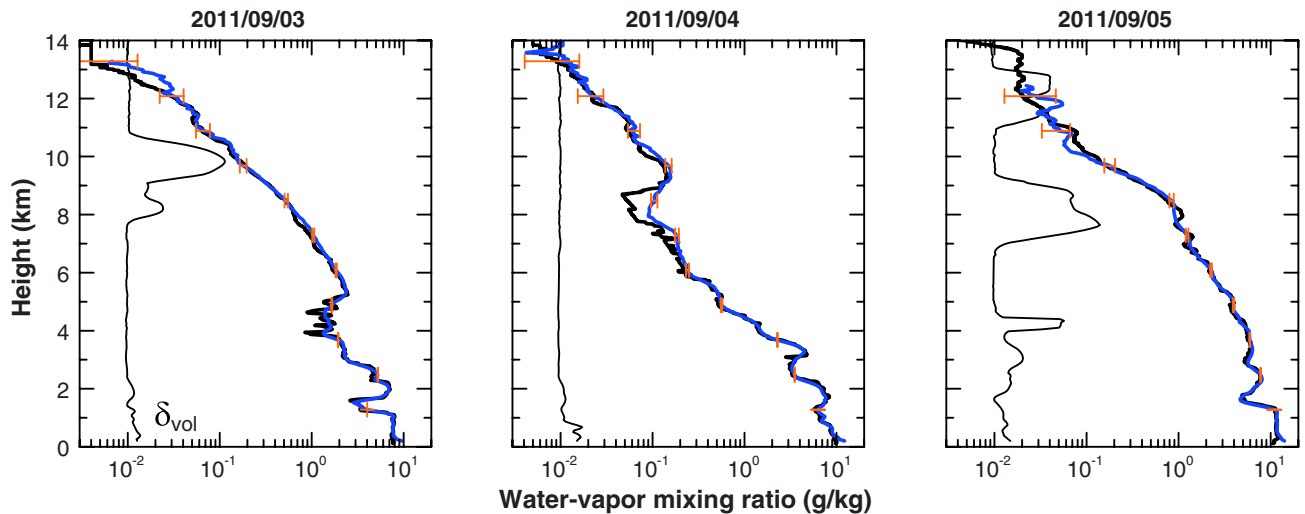


Fig. 13. Profiles of water-vapor MR measured with RAMSES (blue curves) and the midnight radiosondes (black curves) of 3, 4, and 5 September 2011. For each comparison, 1200 s of lidar data are integrated beginning with the launch times of the Lindenberg sondes. Orange bars indicate statistical errors of the lidar measurement. The resolution of the raw data and the sliding-average lengths used for signal smoothing are the same as those of Fig. 12. Above 11 km, sliding-average length increases by two height bins every kilometer. Only data obtained with the far-range receiver are used. Profiles of volume depolarization ratio are presented as indicators of clouds (thin black curves).

profiles obtained with a cryogenic frost-point hygrometer (CFH), which is launched monthly on site as part of the GRUAN activity and which can be regarded as a reference instrument at high altitudes [34]. According to these comparisons, RAMSES profiles show no wet bias. For example, in the night of 22–23 November 2011, the lidar equipped with the experimental hardware listed in Section 2 measured MRs of 2.4–5.9 ppmv in the lower stratosphere (14–16 km) with statistical errors of 2.0–2.5 ppmv, while the CFH yielded height-independent MRs around 5.0 ppmv. RAMSES exhibits even better high-altitude performance after the detector in the far-range water-vapor detection channel was replaced with an improved module based on the Hamamatsu R9880U

tube (Licel) in early 2012 (see Section 6). So it can be concluded that fluorescence does not affect the RAMSES humidity measurements significantly.

Daytime water-vapor measurements of RAMSES on 3 September 2011 are shown in Fig. 14. The profiles compare well with the radiosonde soundings except for the lowest 200 m at noon and in the afternoon. High variability of the water-vapor field near the ground may be the cause for these differences, but instrumental effects like a transient residual error in the overlap correction or electronic disturbances induced by the laser pulse emission cannot be ruled out. In twilight, the maximum measurement range is 7–8 km at 20 min temporal resolution; around noon it drops to about 5.5 km. As the

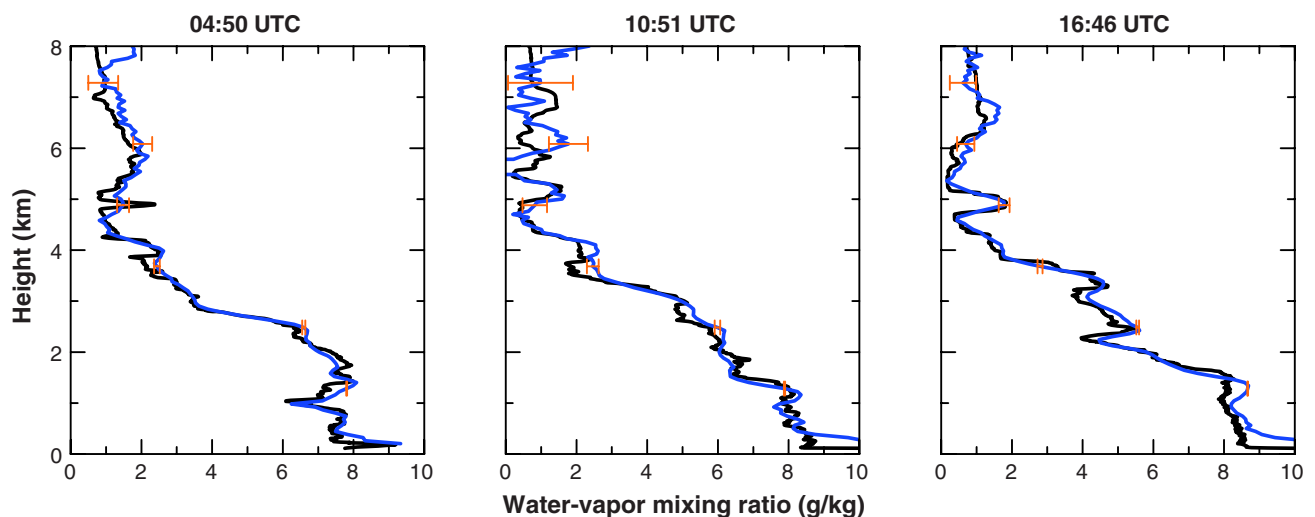


Fig. 14. Profiles of water-vapor MR measured with RAMSES (blue curves) and the three radiosondes launched during daylight (black curves) on 3 September 2011. Clouds were absent below 8 km. For each comparison, 1200 s of lidar data are integrated beginning with the sonde launch times as indicated. Orange bars show statistical errors of the lidar measurement. The resolution of the raw data and the sliding-average lengths used for signal smoothing are the same as those of Fig. 12. Only data obtained with the far-range receiver are used.

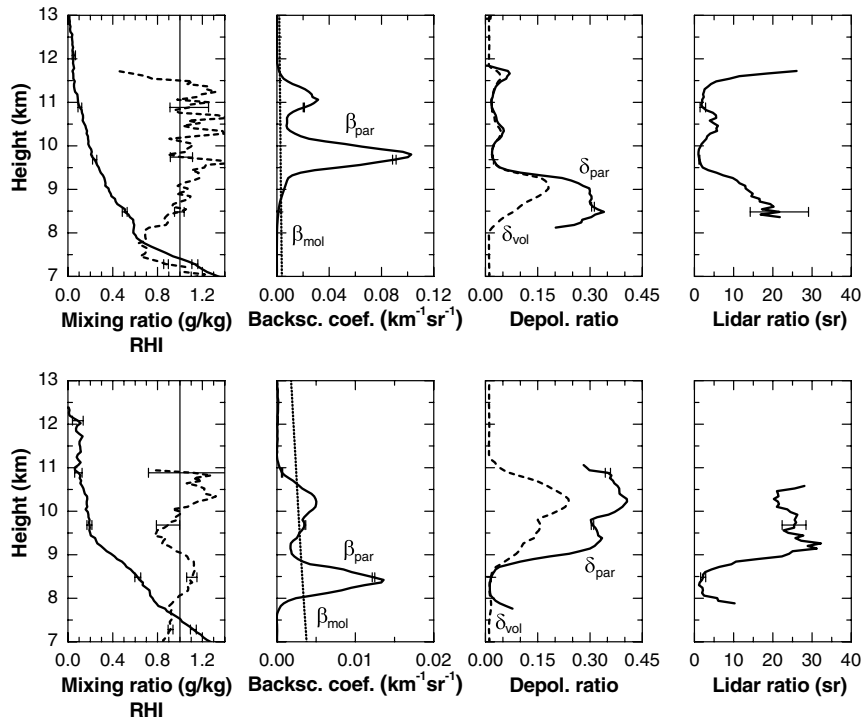


Fig. 15. Water-vapor MR (solid curve) and relative humidity with respect to ice (RHI, dashed curve), particle backscatter coefficient (β_{par} , solid curve), volume and particle depolarization ratios, and lidar ratio as measured with RAMSES during measurement segments M1 (top) and M2 (bottom) of Fig. 12. Bars indicate statistical errors of the lidar measurement. Data integration time is 1200 s. The resolution of the raw data and the sliding-average lengths used for signal smoothing are the same as those of Fig. 12. Molecular backscatter coefficient (β_{mol} , dotted curve) is shown for comparison. Note the different abscissa ranges for the backscatter coefficient.

long-term series shows, these values can be seen as typical of RAMSES' daytime performance when the atmosphere is cloud-free.

Figure 15 presents the measurement segments M1 and M2 marked in Fig. 12. Water-vapor profiles are available throughout the vertical extent of the cirrus clouds, which makes it possible to calculate relative humidity. Considering the statistical errors, the air was saturated with respect to ice within the clouds and subsaturated otherwise. No statistically significant supersaturation was observed, perhaps except for heights around 8.5 km in the M2 case. There are remarkable differences to be observed in the behavior of the particle properties of each measurement segment. In M1, the lidar ratio and the depolarization ratio vary strongly with height and drop from 20 sr and 30% in the cloud bottom layer to minimum values <2 sr and $<2\%$, respectively, at altitudes of maximum cirrus backscattering. During M2, in contrast, both particle properties show high and relative height-constant values of 25 ± 5 sr and 30%–40%, respectively, in the upper cirrus layer, while below lidar ratio and depolarization ratio fall off sharply, again together with an increase in particle backscattering. According to theoretical studies [35], especially low values of the lidar ratio are a sensitive indicator of particle horizontal alignment, so the RAMSES measurements suggest that the cirrus particles were in two-dimensional orientation in these cirrus layers.

Next the cloud-averaged effective diameter of the cirrus particles is estimated from their multiple-scattering effect on lidar temperature measurements with the integration technique. Unlike in previous analyses [36], an elastic backscatter signal (the gated far-range signal of channel E, to be exact) is utilized for the retrieval instead of a vibrational-rotational N_2 Raman signal. The higher signal strength and hence the shorter data integration time make this change in method attractive; however, one has to make sure that the interference with elastic backscattering by stratospheric aerosols is minimized. This is achieved here by choosing a clear-sky Rayleigh-integration temperature measurement close to the cloud observation as the reference profile with which the cloud-affected temperature profile is compared. For an only slowly varying aerosol layer, the aerosol-induced temperature errors then cancel out.

Input to the retrieval algorithm is, among other parameters, the measured extinction-coefficient profile of the cirrus cloud under investigation [36]. Either a microphysically homogeneous cloud or a two-layer cloud can be prescribed. To each layer an effective diameter of the cirrus particles is attributed. Scattering in the forward direction is assumed to follow the phase function of a circular disc of this diameter. This simplification should not affect the retrieval in most cases because it has been shown that cirrus clouds consisting of imperfect or complex ice crystals generate the same forward-scattering lobe

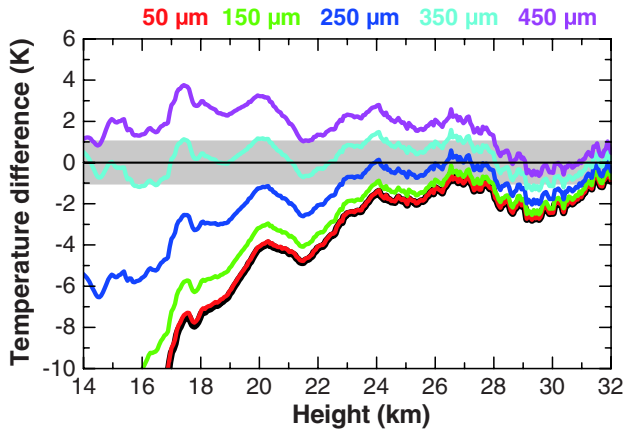


Fig. 16. Differences between the Rayleigh-integration temperature profiles measured during measurement segment M1 and shortly before (00:00–00:20 UTC) under nearly cloud-free conditions. The M1 temperature measurement is either corrected for multiple scattering assuming different effective particle diameters of the cirrus cloud at 8–12 km (colored curves), or not corrected for multiple scattering (black curve). The sliding-average length used for signal smoothing is 1500 m; the starting height for the downward integration is 65 km.

as their counterparts with projection-area equivalent spheres [37]. Model output are the vertical profiles of the higher-order contributions to the lidar return signal which are then used for correcting the Rayleigh-integration temperature profile. Although originally intended for Raman-integration temperature measurements, the model results apply here as well; in ice clouds the multiple-scattering parameters for elastic and Raman backscattering are identical [38].

Figure 16 displays the multiple-scattering analysis of the M1 measurement. With residual temperature differences of less than 1 K after correction, cirrus particles with an effective diameter of 350 μm can explain the observed Rayleigh-integration temperature profile best. Smaller particle sizes yield corrected temperatures that are too cold whereas the assumption of 450 μm particles overestimates the multiple-scattering effect. The assumption of a different particle size in the cirrus layer with predominantly randomly oriented particles below 9.5 km (Fig. 15) does not improve the retrieval results, which suggests that either the effective diameters are similar throughout the cirrus cloud or the horizontally aligned particles in the upper cloud layer are optically dominant. The former explanation is corroborated by the fact that a similar effective diameter is found later on during measurement segment M2 when most of the cloud particles were 3D oriented. This finding suggests that the temporal variations in the optical properties of the cirrus cloud are more the result of changes in the degree of the orientation of its particles than in their microphysical properties. Moreover, if the oriented particles were of plate-like shape, a presumption that is widely accepted, the retrieved effective diameter would actually be close to the effective maximum dimension of the cirrus particles because their length-to-width ratio, or a distribution thereof, would not affect their projection area.

Finally, the stratospheric temperature measurements during the multiday observation period are presented in Fig. 17. Rotational-Raman temperatures are not affected by the presence of particles

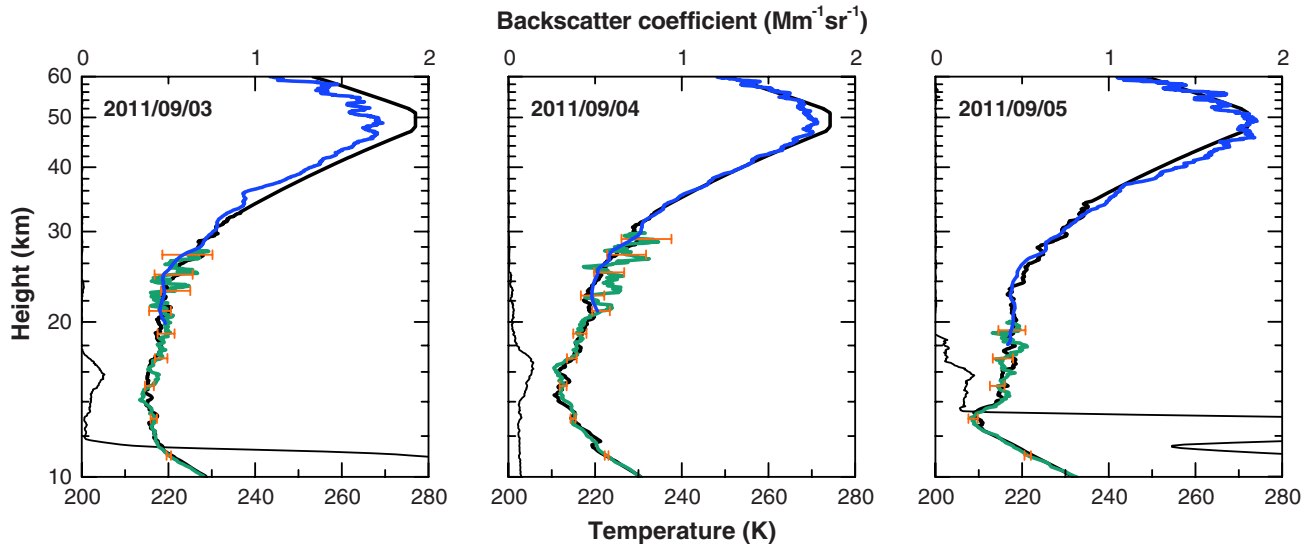


Fig. 17. RAMSES composite profiles of stratospheric temperature (rotational-Raman method, dark cyan curves; Rayleigh-integration method, blue curves) measured during the nights of 2–3, 3–4, and 4–5 September 2011. Starting at 20:50 UTC, 4 h of lidar data are integrated. The sliding-average length is 900 m. Orange bars indicate statistical errors of the rotational-Raman temperature measurement. Start height of the downward integration is 70 km. Temperature profiles of the corresponding midnight radiosondes are shown for comparison (thick black curves). Above the balloon burst heights around 30–35 km, model temperatures are used to extend the profiles upward. Particle backscatter coefficients are presented as indicators of cirrus clouds and stratospheric aerosol (thin black curves). Note the logarithmic height scale.

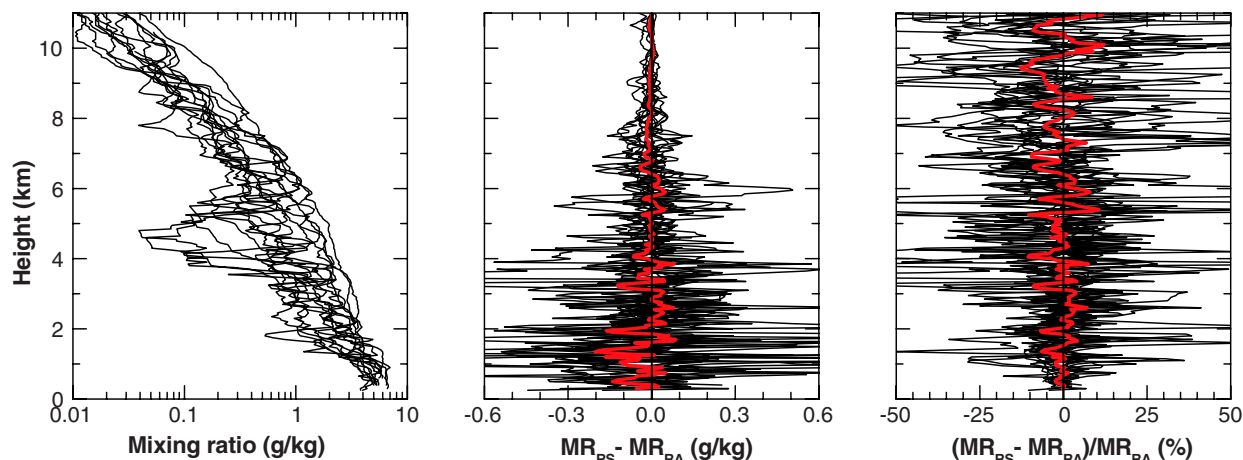


Fig. 18. Statistical comparison between profiles of water-vapor MR measured with RAMSES (MR_{RA}) and routine radiosondes (MR_{RS}) in November 2011 at night. Mean profiles are shown in red. For each lidar profile, 1800 s of data are integrated beginning with the launch times of the Lindenberg sondes. The resolution of the raw data and the sliding-average lengths used for signal smoothing are the same as those of Fig. 12.

nor by multiple scattering and are thus ideal for profiling the troposphere and lower stratosphere. The measurement range varies in this example between 20 and 30 km from night to night, depending on cloudiness. Rayleigh-integration temperatures become available above the stratospheric aerosol layer but only after the intense elastic signal is attenuated enough so that signal nonlinearities are insignificant. As a rule, Rayleigh-integration temperature profiles start at around 20 km, and the measurement range is about 60–70 km under favorable conditions.

B. Statistical Comparisons

For the evaluation of the RAMSES water-vapor performance, it is instructive to compare its measurements to those of other sensors not only for individual profiles but on a statistical basis. This is done routinely using the RS92 radiosonde and, since 2010, the CFH probe. While this analysis is a work in progress and the topic of a followup publication, it can be stated that so far no systematic biases have been found among the instruments. As an example, the comparison between RAMSES and the RS92 radiosonde for November 2011 is presented in Fig. 18. Only night-time measurements under favorable conditions are taken into account. Lidar and sonde agree statistically. The slight mean dry bias of the sonde of -1.5% in the free troposphere (relative to RAMSES) is insignificant. Relevant differences are only seen in humidity filaments with narrow vertical extent where the resolution of the smoothed RAMSES profile is too low to resolve the structure. This sonde-based performance assessment is corroborated by an intercomparison between RAMSES and the airborne water-vapor differential absorption lidar of Deutsches Zentrum für Luft- und Raumfahrt in Oberpfaffenhofen, Germany, during an overflight in October 2008 [39]. Both instruments agreed within 10% to 15% throughout the troposphere without bias [40].

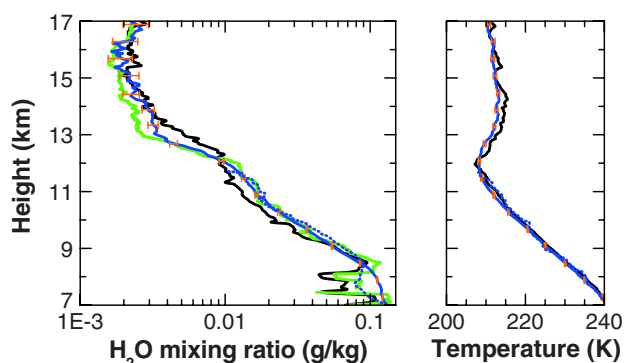


Fig. 19. RAMSES water-vapor and rotational-Raman temperature measurements in the upper troposphere and lower stratosphere in the night of 15–16 March 2012 (solid blue curves). Starting at 19:00 UTC, 8.5 h of lidar data unaffected by astronomical twilight are integrated. The sliding-average length is 900 m below 13 km; above that height it increases by 120 m every kilometer. Orange bars indicate statistical errors. For comparison, profiles measured in situ with a CFH (green curve) and a RS92 radiosonde (black curves, corrected for time lag) are shown. Both sensors (along with others) were attached to a single frame and balloon-launched at 22:52 UTC. Concurrent tropospheric RAMSES profiles are also shown (dotted blue curves, 1200 s integration time).

6. Summary and Outlook

We have presented RAMSES, the fully autonomous Raman lidar of the German Meteorological Service for unattended, continuous multiparameter atmospheric profiling. The optical design concept, the experimental setup, and the operational NRT data evaluation software ALDA have been described in detail. RAMSES is based on a dual-receiver design. The nine-channel far-range polychromator is directly coupled to the main telescope, and the aperture of the primary mirror is imaged onto the detector photocathodes. The three-channel near-range polychromator is fiber-coupled to a secondary telescope, and collimated light is recorded. Water-vapor MR,

temperature, and the optical particle parameters at 355 nm are measured day and night. Temperature profiles of the troposphere and the stratosphere are determined by combining the rotational-Raman technique with the Rayleigh- and Raman-integration techniques. Detection of the rotational Raman signals is accomplished with a new beamsplitter/interference-filter polychromator design that is compact, robust, and easy to align. It was experimentally proven that with this setup temperature measurements are unaffected by particle scattering, e.g., in cirrus clouds with backscatter ratios of at least 60. Two independent calibration methods incorporated in the polychromator allow of accurate measurements of depolarization ratio.

A multiday observation, presented in this paper as an example, demonstrated the satisfactory performance of RAMSES with regard to cloud, water-vapor, and temperature profiling. Profiles of water-vapor MR were measured from close to the surface up to 14 km at night and 5 km during the day in 20 min. Beyond that, comparisons with sonde-borne CFHs show that, under favorable conditions, the measurement range can be extended into the lower stratosphere if RAMSES night-time data are accumulated over several hours. Figure 19 presents the water-vapor and rotational-Raman temperature measurements of the night of 15–16 March 2012 (after PMT upgrade, see Section 5.A) as an example. Clouds were absent and the moonrise (last quarter) was late in the night. Lidar and sonde profiles agree well up to 17 km. With such a performance, RAMSES ranks among the premier water-vapor Raman lidars worldwide [11].

Daytime water-vapor capability is limited by the temperature stability of the instrument cabin, which proved to be insufficient for measurements with narrow FOV, particularly in summer. Active overlap stabilization is helpful in this context, but the temperature effect still requires $\text{FOV} > 0.35$ mrad. A significant performance improvement can thus be expected after RAMSES is moved into the new lidar facility with precision air conditioning, which is currently under construction on site, and a narrower FOV can be selected. RAMSES is considered to participate in the Network for the Detection of Atmospheric Composition Change [8], in addition to its main tasks, i.e., DWD uses and contributions to GRUAN activities.

The authors thank Volker Freudenthaler for his valuable recommendations on lidar system design made in the context of the EARLINET quality-assurance program. The assistance of Oliver Reitebuch in the measurement of the laser wavelength is acknowledged. The authors thank Holger Vömel and the in situ sounding team at Lindenberg for the sonde data of 15 March 2012.

References

1. U. Wandinger, "Raman lidar," in *Lidar: Range-Resolved Optical Remote Sensing of the Atmosphere*, C. Weitkamp, ed. (Springer, 2005), pp. 241–271.

2. A. Ansmann, M. Riebesell, U. Wandinger, C. Weitkamp, E. Voss, W. Lahmann, and W. Mischealis, "Combined Raman elastic-backscatter lidar for vertical profiling of moisture, aerosol extinction backscatter, and lidar ratio," *Appl. Phys. B* **55**, 18–28 (1992).
3. D. N. Whiteman, S. H. Melfi, and R. A. Ferrare, "Raman lidar system for the measurement of water vapor and aerosols in the Earth's atmosphere," *Appl. Opt.* **31**, 3068–3082 (1992).
4. J. Reichardt, U. Wandinger, M. Serwazi, and C. Weitkamp, "Combined Raman lidar for aerosol, ozone, and moisture measurements," *Opt. Eng.* **35**, 1457–1465 (1996).
5. J. E. M. Goldsmith, F. H. Blair, S. E. Bisson, and D. D. Turner, "Turn-key Raman lidar for profiling atmospheric water vapor, clouds, and aerosols," *Appl. Opt.* **37**, 4979–4990 (1998).
6. V. Sherlock, A. Garnier, A. Hauchecorne, and P. Keckhut, "Implementation and validation of a Raman lidar measurement of middle and upper tropospheric water vapor," *Appl. Opt.* **38**, 5838–5850 (1999).
7. D. Althausen, D. Müller, A. Ansmann, U. Wandinger, H. Hube, E. Clauder, and S. Zörner, "Scanning 6-wavelength 11-channel aerosol lidar," *J. Atmos. Ocean. Technol.* **17**, 1469–1482 (2000).
8. T. Leblanc, I. S. McDermaid, and R. A. Aspey, "First-year operation of a new water vapor Raman lidar at the JPL Table Mountain Facility, California," *J. Atmos. Ocean. Technol.* **25**, 1454–1462 (2008).
9. P. Di Girolamo, D. Summa, and R. Ferretti, "Multiparameter Raman lidar measurements for the characterization of a dry stratospheric intrusion event," *J. Atmos. Ocean. Technol.* **26**, 1742–1762 (2009).
10. A. Apituley, K. M. Wilson, C. Potma, H. Volten, and M. de Graaf, "Performance assessment and application of Caeli—a high-performance Raman lidar for diurnal profiling of water vapour, aerosols and clouds," in *Proceedings of the 8th International Symposium on Tropospheric Profiling: Integration of Needs, Technologies and Applications*, A. Apituley, H. W. J. Russchenberg, and W. A. A. Monna, eds. (2009), paper S06-O10.
11. T. Leblanc, T. D. Walsh, I. S. McDermaid, G. C. Toon, J.-F. Blavier, B. Haines, W. G. Read, B. Herman, E. Fetzer, S. Sander, T. Pongetti, D. N. Whiteman, T. G. McGee, L. Twigg, G. Sumnicht, D. Venable, M. Calhoun, A. Dirisu, D. Hurst, A. Jordan, E. Hall, L. Miloshevich, H. Vömel, C. Straub, N. Kampfer, G. E. Nedoluha, R. M. Gomez, K. Holub, S. Gutman, J. Braun, T. Vanhove, G. Stiller, and A. Hauchecorne, "Measurements of Humidity in the Atmosphere and Validation Experiments (MOHAVE)-2009: overview of campaign operations and results," *Atmos. Meas. Tech.* **4**, 2579–2605 (2011).
12. T. Dineev, P. Ristori, Y. Arshinov, S. Bobrovnikov, I. Serikov, B. Calpini, H. van den Bergh, and V. Simeonov, "Meteorological water vapor Raman lidar—advances," *Proc. SPIE* **6367**, U98 (2006).
13. D. Engelbart, J. Reichardt, I. Mattis, U. Wandinger, V. Klein, A. Meister, B. Hilber, and V. Jaenisch, "RAMSES—German Meteorological Service Raman lidar for atmospheric moisture sensing," in *Reviewed and Revised Papers Presented at the 23rd International Laser Radar Conference*, C. Nagasawa and N. Sugimoto, eds. (2006), pp. 683–686.
14. F. H. Berger, J. Reichardt, A. Beljaars, J. Güldner, and C. Heret, "Evaluation of modeled water vapour profiles using Raman lidar data," in *Proceedings of the 8th International Symposium on Tropospheric Profiling: Integration of Needs, Technologies and Applications*, A. Apituley, H. W. J. Russchenberg, and W. A. A. Monna, eds. (2009), paper S07-O05.
15. H. Woick, S. Dewitte, A. Feijt, A. Gratzki, P. Hechler, R. Hollmann, K.-G. Karlsson, V. Laine, P. Löwe, H. Nitsche, M. Werscheck, and G. Wollenweber, "The Satellite Application Facility on climate monitoring," *Adv. Space Res.* **30**, 2405–2410 (2002).
16. D. J. Seidel, F. H. Berger, H. J. Diamond, J. Dykema, D. Goodrich, F. Immler, W. Murray, T. Peterson, D. Sisterson, M. Sommer, P. Thorne, H. Vömel, and J. Wang, "Reference upper-air observations for climate: rationale, progress, and plans," *Bull. Am. Meteorol. Soc.* **90**, 361–369 (2009).

17. J. Reichardt, D. Engelbart, U. Wandinger, I. Mattis, V. Klein, and B. Hilber, "Expansion of the German Meteorological Service Raman Lidar RAMSES," in *Proceedings of the 8th International Symposium on Tropospheric Profiling: Integration of Needs, Technologies and Applications*, A. Apituley, H. W. J. Russchenberg, and W. A. A. Monna, eds. (2009), paper S06-P06.
18. J. Reichardt, R. Begbie, U. Wandinger, V. Klein, B. Hilber, and D. Engelbart, "First water vapor and cloud measurements with the new far-range receiver of the German Meteorological Service Raman lidar RAMSES," in *Proceedings of the 25th International Laser Radar Conference*, G. Matvienko and A. Zemlyanov, eds. (2010), pp. 1179–1182.
19. R. K. Newsom, D. D. Turner, B. Mielke, M. Clayton, R. Ferrare, and C. Sivaraman, "Simultaneous analog and photon counting detection for Raman lidar," *Appl. Opt.* **48**, 3903–3914 (2009).
20. V. Simeonov, G. Larcheveque, P. Quaglia, H. van den Bergh, and B. Calpini, "Influence of the photomultiplier tube spatial uniformity on lidar signals," *Appl. Opt.* **38**, 5186–5190 (1999).
21. V. Freudenthaler, "Effects of spatially inhomogeneous photomultiplier sensitivity on lidar signals and remedies," in *Proceedings of the 22nd International Laser Radar Conference* (ESA Publications Division, 2004), SP-561, pp. 37–40.
22. D. N. Whiteman, I. Veselovskii, M. Cadirola, K. Rush, J. Comer, J. R. Potter, and R. Tola, "Demonstration measurements of water vapor, cirrus clouds, and carbon dioxide using a high-performance Raman lidar," *J. Atmos. Ocean. Technol.* **24**, 1377–1388 (2007).
23. J. M. Alvarez, M. A. Vaughan, C. A. Hostetler, W. H. Hunt, and D. M. Winker, "Calibration technique for polarization-sensitive lidars," *J. Atmos. Ocean. Technol.* **23**, 683–699 (2006).
24. J. Reichardt, R. Baumgart, and T. J. McGee, "Three-signal method for accurate measurements of depolarization ratio with lidar," *Appl. Opt.* **42**, 4909–4913 (2003).
25. J. Reichardt, "Raman backscatter-coefficient spectra of cirrus ice," in *Reviewed and Revised Papers of the 26th International Laser Radar Conference*, A. Papayannis, D. Balis, and V. Amiridis, eds. (2012), pp. 387–390.
26. I. Mattis and V. Jaenisch, "Automated Lidar Data Analyzer (ALDA) for RAMSES—the autonomously operating German Meteorological Service Raman lidar for atmospheric moisture sensing," in *Reviewed and Revised Papers Presented at the 23rd International Laser Radar Conference*, C. Nagasawa and N. Sugimoto, eds. (2006), pp. 215–218.
27. D. Whiteman, "Examination of the traditional Raman lidar technique. I. Evaluating the temperature-dependent lidar equations," *Appl. Opt.* **42**, 2571–2592 (2003).
28. L. Elterman, "UV, visible, and IR attenuation for altitudes to 50 km, 1968," environmental research papers AFCRL-68-0153, Air Force Cambridge Research Laboratories, L. G. Hanscom Field, Bedford, Massachusetts (1968).
29. P. M. Teillet, "Rayleigh optical depth comparisons from various sources," *Appl. Opt.* **29**, 1897–1900 (1990).
30. A. Behrendt and J. Reichardt, "Atmospheric temperature profiling in the presence of clouds with a pure rotational Raman lidar by use of an interference-filter-based polychromator," *Appl. Opt.* **39**, 1372–1378 (2000).
31. A. Ansmann and D. Müller, "Lidar and atmospheric aerosol particles," in *Lidar: Range-Resolved Optical Remote Sensing of the Atmosphere*, C. Weitkamp, ed. (Springer, 2005), pp. 105–141.
32. A. Ansmann, U. Wandinger, O. Le Rille, D. Lajas, and A. Straume, "Particle backscatter and extinction profiling with the spaceborne HSR Doppler lidar ALADIN: methodology and simulations," *Appl. Opt.* **46**, 6606–6622 (2007).
33. D. N. Whiteman, K. Rush, S. Rabenhorst, W. Welch, M. Cadirola, G. McIntire, F. Russo, M. Adam, D. Venable, R. Connell, I. Veselovskii, R. Forno, B. Mielke, B. Stein, T. Leblanc, S. McDermaid, and H. Vömel, "Airborne and ground-based measurements using a high-performance Raman lidar," *J. Atmos. Ocean. Technol.* **27**, 1781–1801 (2010).
34. H. Vömel, D. E. David, and K. Smith, "Accuracy of tropospheric and stratospheric water vapor measurements by the cryogenic frost point hygrometer: Instrumental details and observations," *J. Geophys. Res.* **112**, D08305 (2007).
35. J. Reichardt, S. Reichardt, R.-F. Lin, M. Hess, T. J. McGee, and D. O. Starr, "Optical-microphysical cirrus model," *J. Geophys. Res.* **113**, D22201 (2008).
36. J. Reichardt and S. Reichardt, "Determination of cloud effective particle size from the multiple-scattering effect on lidar integration-method temperature measurements," *Appl. Opt.* **45**, 2796–2804 (2006).
37. J. Reichardt, M. Hess, and A. Macke, "Lidar inelastic multiple-scattering parameters of cirrus particle ensembles determined with geometrical-optics crystal phase functions," *Appl. Opt.* **39**, 1895–1910 (2000).
38. U. Wandinger, "Multiple-scattering influence on extinction- and backscatter-coefficient measurements with Raman and high-spectral-resolution lidars," *Appl. Opt.* **37**, 417–427 (1998).
39. M. Wirth, A. Fix, G. Ehret, J. Reichardt, R. Begbie, D. Engelbart, H. Vömel, B. Calpini, G. Romanens, A. Apituley, K. M. Wilson, H. Vogelmann, and T. Trickl, "Intercomparison of airborne water vapour DIAL measurements with ground based remote sensing and radiosondes within the framework of LUAMI 2008," in *Proceedings of the 8th International Symposium on Tropospheric Profiling: Integration of Needs, Technologies and Applications*, A. Apituley, H. W. J. Russchenberg, and W. A. A. Monna, eds. (2009), paper S07-P01.
40. M. Wirth, DLR Oberpfaffenhofen, Weßling, Germany, personal communication (2012).